MTLA 33 (2024) 102033

Contents lists available at ScienceDirect

Materialia

journal homepage: www.elsevier.com/locate/mtla

Full length article

On a mathematical theory for the crystallography of shear transformations in metals: Unification of mechanisms

Enrique Galindo-Nava

Department of Mechanical Engineering, University College London, Torrington Place, London, WC1E 7JE, UK

ARTICLE INFO

Keywords:
Martensite
Crystallography
Orientation relationship
Modelling
Steel

ABSTRACT

A theory for shear transformations in crystalline materials linking their Crystallography, atomic-scale mechanisms and Thermodynamics is introduced. The lattice and transformation function are treated as vector space and functions respectively to overcome shortcomings of classical matrix-based theories for martensite crystallography. The extremum principle is used to obtain the atomic paths minimising and maximising the energy from all possible solutions, therefore explaining which sequences are more Thermodynamically feasible. The face-centred cubic (FCC)→body-centred cubic (BCC) transformation in Fe is used as case study. The theory predicts that the average values of the extrema correspond to the crystallography, shear magnitude, interface defects and habit planes of main transformations in Fe, *i.e.* Widmanstätten Ferrite, Bainite, lath martensite, plate and lenticular martensite. Bainite represents the macroscopic average minimum energy configuration, whereas Widmanstätten Ferrite corresponds to a local and discrete minimum energy configuration. Lath martensite corresponds to the average shear configurations minimising atomic displacements when there is no other driving force, *e.g.* diffusion, whereas the maximum energy configurations correspond to plate and lenticular martensite forming twin pairs. Targeted results for the FCC→hexagonal close-packed lattice transformation are presented to demonstrate the robustness of the theory. The predictions are combined with elasticity theory to compute the Driving Force and predict the start temperatures – therefore connecting for the first time – local and macroscopic crystallographic features with the Thermodynamics of shear-controlled structures in Fe. This work presents new results towards addressing longstanding challenges in Materials Science such as theoretically demonstrating that Bainite is a shear transformation.

1. Introduction

It has been more than 100 years since the discoveries of martensite (1890s) and bainite (1920s) in iron [1,2]. Since then, steels and other materials utilising shear transformations have been developed to deliver unique properties, such as high strength, toughness, the so-called "shape memory effect", elastocaloric response, among others [3,4]. These transformations occur by rapid and coordinated atomic displacements commonly leaving a one-to-one atomic correspondence – or orientation relationship (OR) – between the parent and product phase. In spite of the great importance of shear transformations in Materials Science, to date, there is no unified theory able to predict and explain from first principles the connections between Crystallography, Thermodynamics and atomic mechanisms of different transformations. This limitation also echoes longstanding debates in the Materials Science community, such as the bainite controversy, *i.e.* whether it is a diffusion -or shear controlled transformation. Experimental evidence supports the view of bainite being a shear transformation, although promoted by atomic diffusion, but there is no quantitative theory able to justify the empirical knowledge [5]. Similarly for other material systems, there are longstanding inconsistencies reported in the crystallography of materials undergoing various shear transformations, *e.g.* for Titanium, NiTi and ZrO-based shape memory alloys/ceramics [6–9]. In this context, one may even ask a more fundamental question: why allotropic materials can undergo multiple transitions for a given chemical composition, *e.g.* for Fe and steel, Widmanstätten Ferrite, Bainite, lath, plate (twinned) and lenticular martensite? In addition, it is widely acknowledged that experimentally measured orientation relationships (ORs) do not correspond exactly to classical ORs [10], namely for Fe Bain (B), Kurdjumov–Sachs (KS), Nishiyama–Wasserman (NW), Pitsch (P) and Greninger–Troiano (GT) (Table 1). Instead, it has been shown that the transformation variants form a continuum trajectory between KS, NW, P and GT ORs [7,11] and different atomic paths should lead to the same OR during the transformation.

Given the importance of shear transformations in Materials Science, several approaches have been proposed and validated – to a degree – throughout the years. Most eminently, the Phenomenological Theory

E-mail address: e.galindo-nava@ucl.ac.uk.

https://doi.org/10.1016/j.mtla.2024.102033
Received 27 October 2023; Accepted 12 February 2024
Available online 21 February 2024

Table 1
Different ORs between FCC and BCC crystals.

OR	Direction parallel	Plane parallel	Variants
Bain (B)	$\langle 100\rangle_{FCC}\|\|\langle 110\rangle_{BCC}$	$\{100\}_{FCC}\|\|\{100\}_{BCC}$	3
Kurdjumov–Sachs (KS)	$\langle 1\bar{1}0\rangle_{FCC}\|\|\langle 111\rangle_{BCC}$	$\{111\}_{FCC}\|\|\{110\}_{BCC}$	24
Nishiyama–Wasserman (NW)	$\langle 1\bar{1}0\rangle_{FCC}\|\|\langle 100\rangle_{BCC}$	$\{111\}_{FCC}\|\|\{110\}_{BCC}$	12
Pitsch (P)	$\langle 1\bar{1}0\rangle_{FCC}\|\|\langle 111\rangle_{BCC}$	$\{100\}_{FCC}\|\|\{110\}_{BCC}$	12
Greninger–Troiano (GT)	$\langle 2\bar{1}1\rangle_{FCC}\|\|\langle 101\rangle_{BCC}$	$\{111\}_{FCC}\|\|\{110\}_{BCC}$	24

of Martensite Crystallography (PTMC) [12] with further improvements and generalisations [13–16]. More recently, Cayron and co-workers have approached the problem differently [17–20] by considering atoms as hard spheres and defining a distortion matrix for the required transformation atomic paths that is consistent with the associated crystallography. Although these theories have been successfully used to explain several transformations in Fe and other materials, most cannot explain the specific atomic mechanisms involved and they cannot be linked with the transformation Thermodynamics and/or kinetics to be able to predict the resulting microstructure; similarly, these approaches are not able to explain why multiple diffusionless and diffusion-controlled transformations happen in the same material. Interface models, such as the topological and Edge-to-edge matching models [21–26], have also been proposed to explain the crystallography of parent/product interphases and identify defects (mainly dislocations) required to minimise the interfacial strain energy but they do not explicitly address the atomic mechanisms involved in the transformation or cover other defects commonly observed in shear transformations like twinning. Atomistics such as Ab initio methods have been used to study ground states between FCC and BCC/BCT martensite in Fe but the increased computational complexities allow to only cover very small supercells [27]. This limits the study of phase transitions which require distorted intermediate states, as in the case of shear transformations, as finite size effects can become dominant. On the other hand, Molecular Dynamics has been a popular method to study martensite in Fe [28], *e.g.* for linking ORs when martensite nucleates at different interfaces, but results vary significantly for different simulation setups and only K–S and N–W ORs have been reported. A central problem has been that most interatomic potentials for the FCC→BCC phase transformation have been obtained from fitting atomic displacements along the Bain path and using results from the PTMC, therefore limiting their predictability given the known shortcomings of the PTMC. In addition, MD is not suitable to study diffusion-influenced transformations such as the bainitic reaction due to the long times required (>ms). In summary, there are many outstanding challenges in classical and more recent theories for the crystallography of martensite and other shear transformations and there is genuine value in revisiting these approaches to seek for definite answers.

The aim of this paper is to introduce a mathematical formalism – as alternative approach to classical theories – to simultaneously describe the Crystallography, atomic paths and Thermodynamics of shear transformations based on a generalised lattice theory using vector theory and the extremum principle. Section 2 covers the Background where main limitations of the Matrix-theory based Phenomenological Theory of Martensite Crystallography are identified. The problem is later "re-defined" in terms of vector theory in Section 3 and it is shown that atomic displacements are better illustrated as vector trajectories. This, in combination with the Extremum principle, not only helps in making the transformation processes easier to "visualise" but also to highlight key physical processes and the energetics behind a shear–influenced transformation. The FCC→BCC crystal transformation in Fe is used as case study in Section 3.3 to illustrate the principles of the theory for the predefined ORs KS and NW; the results are successful in predicting the local crystallography and defect formation of Fe's main shear transformations, *i.e.* Widmansttätten Ferrite, Bainite, lath martensite, as well as plate and lenticular martensite. The theory is generalised in Section 4 to predict local and average crystallographic features of all shear transformations in Fe, including the prediction of other ORs between FCC and BCC, *i.e.* Pitsch, Greninger–Troiano and Bain, as well as identification of specific atomic paths for different transformation variants. Targeted results for FCC→HCP crystals are also discussed in this section to demonstrate the robustness of the theory. The specifics of this transformation are successfully recovered in terms of the local driving force and dislocation configurations necessary for the phase transition. Section 5 derives the links between the Crystallography and Thermodynamics of the transformations to compute the driving force of all predicted structures. Summary and concluding remarks are presented in Section 6 highlighting the cornerstone novelties of the present integrated approach and scientific questions it has successfully addressed.

2. Towards a mathematical theory for the crystallography of shear transformations

Background

So far, the most widely used and accepted approach to explain the crystallography of martensitic and other shear transformations has been the Phenomenological Theory of Martensite Crystallography and its multiple variations [14,15,29]. It is not the aim of this work to extensively discuss its main features and criticisms, as there are other reviews readily available, but to highlight key assumptions that – in the author's opinion – are the primary reasons of the lack in meaningful progress in explaining the crystallography and atomic mechanisms of any shear transformation using a general approach, *e.g.* it was only until 2017 that the atomic paths leading to the crystallographic features of {225} habit plane in plate (twinned) martensitic steels were successfully explained, more than 60 years after the conception of the PTMC [19].

The basic idea of the PTMC is that the transformation strain tensor (matrix) P is composed by the product of a lattice deformation tensor B – or Bain strain – also generating the product lattice from the parent lattice-, a number of lattice invariant deformation tensor(s) S and a rigid body rotation R. This is mathematically expressed as [29,30]:

$$P = RBS. \tag{1}$$

We highlight here that matrix multiplication is in general non-commutative and requires predefining a transformation sequence, *i.e.* invariant deformation happens before (S) lattice deformation (B), although in reality both processes may happen simultaneously. It is later noted that P can be instead represented by a simple shear relationship assuming P is an invariant plane strain: $P = I + m\boldsymbol{d}\boldsymbol{p}^T$ where m is the shear magnitude, $\boldsymbol{d}$ is the normalised shear direction, $\boldsymbol{p}$ the normalised habit plane, and ^{T} denotes its transpose. $\boldsymbol{d}$ for Fe is assumed to be composed either by dislocations or twin variants. Variations of this theory follow similar solution methods.

Three main shortcomings to address in the PTMC are:

1. Pre-existence of crystal defects is always needed to explain the strain accommodation process and compute $\boldsymbol{d}$ but the origins of why and how such defects form is not established. This is because – for instance in the case of Fe – the Bain correspondence requires the addition of slip and twinning to be able to reproduce the right shape and structure. In addition, there is no

quantitative explanation what forms first, the predicted ORs or the pre-defined defects – or if both form simultaneously – and any geometric links between these two features.
2. No direct connection between the Crystallography and Thermodynamics of the transformation, *e.g.* via predicting the start temperatures (M_s, B_s, etc.), which does not make possible to relate features of different transformations in the same material, *e.g.* explain why twins and dislocations are predominant in plate and lath martensite, respectively. This also implies that it is not possible to explain using this theory why different allotropic phases happen to the same material following different thermal/mechanical histories.
3. Most theories are Matrix based and follow linear algebra concepts. This formalism, although mathematically correct, does require predefining specific sequences in the transformation as matrix multiplication is in general non-commutative, *i.e.* invariant transformation happens before lattice deformation, but shear transformations are not symmetric. In addition, for lattices with lower symmetry such as the HCP, a single 3 × 3 matrix is not able to describe all necessary crystal lattice symmetries and additional considerations are needed to make a phase transformation function complete.

Item 1 is a key assumption for all models and is the main reason why most approaches are Phenomenological. Referring to Bowles and Mackenzie's seminal paper, they stated [12]: "the theory is phenomenological and is concerned only with the initial and final states. It follows that nothing can be deduced about the actual paths taken by the atoms during transformation". Although subsequent works tried to expand the scope of the theory *e.g.* by incorporating multiple shear processes [29], so far no work has been able to predict and explain why crystal defects form in the first place, *i.e.* whether they form before or during the phase transformation, and why dislocations and twins form specifically in lath and plate/lenticular martensite in Fe, respectively. Such information could give meaningful clues about how the microstructure evolves during the transformation process. In addition, experimental evidence has highlighted that selection of specific ORs and formation of crystal defects may happen simultaneously, suggesting that crystal defects form as the transformation happens and not before (item 2). In-situ TEM studies on deformation-induced martensite in Fe have shown that the selection of the crystallographic variant for the martensite nucleus was not related to the accommodation of transformation strain by dislocations in the austenite [31–34]; it was also shown that preexisting defects in austenite are not transmitted to martensite and the internal martensite microstructure and interface evolve independently. As for predefining the ORs, a number of models have been proposed to predict ORs based on energy minimisation arguments [35], such as minimising the misfit at the interface [25,36], but these have not been able to predict the occurrence of defects or have been linked to the driving force of the transformation. Overcoming this limitation could allow us to study different ORs simultaneously and explain why several ORs are observed in the same transformation structure -a current limitation in the PTMC and other existing approaches- and that there are continuum paths between them.

For item 2, the PTMC was originally defined to study martensitic transformations but it has been applied to other shear transformations such as twinning, Widmansttätten Ferrite, etc., however, there is not proper mathematical justification of why it works in these cases, *i.e.* there is no (Energy-based) criterion that determines the atomic sequences more favourable in each case. As consequence, the PTMC cannot explain why several allotropic transformations with different crystallographic features can occur in the same material system, *e.g.* Widmansttätten Ferrite, Bainite and multiple martensites in Fe, as it is not possible to connect the predictions to specific atomic paths of different structures and their associated driving forces. When looking at other materials such as Ti and Shape Memory alloys, the existence of multiple allotropic transformations within a single material composition is common but these theories fail to predict and explain their occurrence.

As for item 3, referring again to Bowles and Mackenzie's paper: "since the problem is concerned with finite, though small, homogeneous strains a matrix representation is appropriate". This assumption has subtle but significant consequences as the transformation strain in many metals like Fe is very high (≥ 0.2) [29]; this will be addressed in the following sections. Most Matrix-based representations have not considered atomic displacements, which leads to inconsistencies in the theory or to introduce ill-defined physical concepts such as "atomic shuffles". For instance, when calculating the crystallography of FCC→HCP transition in FeMnSi using the PTMC, Guo et al. [37] had to assume small "atomic shuffles" occurring in the middle layer of an FCC plane but without affecting the macroscopic shape cell in order to recover the HCP shape. The concept of "atomic shuffling" has no clear physical justification — nor mechanisms for its occurrence [38]. Similar arguments have been reported for the FCC→HCP→BCT phase transformations [33] where small atomic shuffles are required – in addition to forming Shockley partials – to complete the transformation sequence. Cayron [18] partially overcame this problem by using a hard-sphere model. Distortion matrices are computed to represent specific atomic displacements along various ORs, via the angle of planar distortion, but it is not known if these specific paths correspond to minimum/maximum energy paths, as there are infinite number of possible atomic configurations for the FCC→BCC phase transition. Although matrix multiplication to a vector is equivalent to performing a linear transformation on that vector – which can prove to be useful when deconvoluting several transformations, *e.g.* dilation, pure shear and rotation – the fact that matrix multiplication is not commutative means that careful attention about product order is needed. Another example of why Matrix based approaches are not always convenient is that a single shear matrix may not be able to predict all crystallographic features, *e.g.* the only way the PTMC could predict the habit plane {755} in lath martensite was by introducing 2 IPS. To the author's knowledge, the requirement of having 2 IPS has not been explained using theoretical arguments, but instead the fact that either dislocations or twins are observed in martensite, hence these are simply assumed to be strain accommodation components.

All this demonstrates that there is significant merit in approaching the problem differently with the aim of gaining more insights about unanswered – or at partially answered – questions concerning the crystallography and Thermodynamics of shear transformations. The aim of the work is to introduce an alternative theoretical approach with main assumptions simple and easy to understand, yet with a mathematical formalism robust enough to address issues that existing theories could not address before. In addition, we will show that main features of the approach are compatible with existing theories, like the PTMC, whilst explaining why the present theory is able to explain more compellingly the physics behind shear transformations.

3. Basic definitions: Crystal lattice and shear transformation functions

We will introduce an alternative approach to describe shear transformations using lattice and vector theories. We will only make brief comparisons and analogies to the PMTC since this work is based on different assumptions and mathematical formalism that guarantee the theory is complete. Further discussion and possible links to the PTMC are presented in Section 5.1.

3.1. Revisiting lattice theory

A simple definition of a crystal lattice, *i.e.* a periodic arrangement of atoms forming a crystal, gives the classical mathematical interpretation of any lattice point A being identified using a set of 3 basis vectors

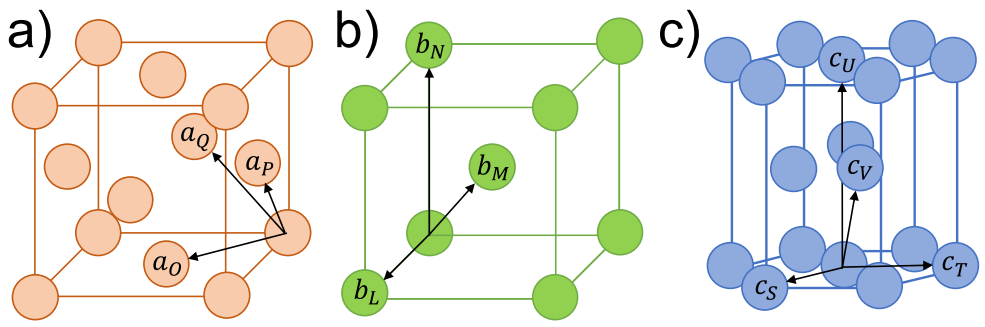

Fig. 1. Primitive vectors considered in the (a) FCC, (b) BCC and (c) HCP lattice systems.

$a_i \in \mathbb{R}^3$ [39]: $A = Oa_1 + Pa_2 + Qa_3$, where O, P, Q are integers representing the lattice's translational symmetry. The parallelepiped constructed from a_i forms a unit cell and, for convenience, the basis vectors are typically chosen to form a primitive (reduced) cell forming the motif. We must note that a crystal lattice is formed by the lattice and the motif, with both features fully describing crystal symmetry. Mathematically, this means that if the primitive unit cell does not match the motif, it may not be possible to span the crystal lattice using only 3 vectors. For example, the motif of the HCP lattice is given by a rhombic prism having 4 atoms outside the origin (c_S, c_T, c_U and c_V) in Fig. 1(c), and 3 basis vectors (lattice points) are not enough to generate this motif. Referring to Fig. 1c, if the lattice basis vectors are (in cartesian coordinates): $c_S = a_\epsilon[1,0,0]$, $c_T = a_\epsilon[-\frac{1}{2}, \frac{\sqrt{3}}{2}, 0]$ and $c_U = a_\epsilon[0,0,\omega]$, where $\omega = \frac{c_\epsilon}{a_\epsilon}$, it is impossible to obtain the lattice point $c_V = \frac{a_\epsilon}{2}[1, \frac{1}{\sqrt{3}}, \omega]$ using linear combinations of c_S, c_T and c_U with only integer coefficients, *i.e.* $c_V \neq Sc_S + Tc_T + Uc_U$ for $S, T, U \in \mathbb{Z}$. In fact, it is easy to show that there is no combination of 3 basis vectors that can span every atom in the HCP lattice using integer coefficients because the motif requires 4 vector coordinates to completely describe its crystal symmetries. Other lattices with similar issues include ordered structures, such as ZrO or NiTi, where atoms of different species occupy specific lattice points and additional basis vectors are needed to describe this difference. This subtle but important limitation when using a classical mathematical treatment has crucial implications towards defining accurate vector functions representing phase transformations. This is because in shear transformations there must exist a one-to-one correspondence between lattice points in the parent and product phases, *i.e.* the transformation function must be injective. For example, 3×3 matrices can only represent 3 atomic positions to predict lattice symmetry, which is not enough to completely determine the motif, hence all atomic positions and crystal symmetries in the HCP lattice. We will therefore proceed to modify slightly the previous mathematical framework and treat the crystal lattice as a vector space but with a more general formalism.

We now assume that a crystal lattice $\mathcal{A}$ is generated by N linearly independent vectors $a_i \in \mathbb{R}^3$ with $i = 0, 1, \ldots, N-1$, where N is the minimum number of primitive vectors to generate the motif in $\mathcal{A}$, such that any lattice point $A \in \mathcal{A}$ is obtained by their linear combination:

$$A = \sum_{i=0}^{N-1} N_i a_i \tag{2}$$

where $N_i \in \mathbb{Z}$. It is important to note that this generalised definition preserves the translational symmetry of the lattice as required. An advantage of this definition is that we can also define the dimension of any lattice as $\dim(\mathcal{A}) = N$. This number is defined as the number of vectors (or lattice points) required to generate the motif of a crystal structure, it does not refer to a spatial dimension which is always 3-dimensional. Identifying N is important because the dimension (or motif) of the parent and product phases after a phase transformation are not necessarily identical, *e.g.* $N = 3$ for the FCC and BCC lattices but $N = 4$ in the HCP lattice as just discussed, and additional considerations

Table 2
Primitive vectors considered in this work for various crystal structures.

FCC	BCC	HCP
$a_O = \frac{a_\epsilon}{2}[1,-1,0]$	$b_M = \frac{a_\alpha}{2}[1,1,1]$	$c_S = a_\epsilon[1,0,0]$
$a_P = \frac{a_\epsilon}{2}[1,0,1]$	$b_N = a_\alpha[0,0,1]$	$c_T = a_\epsilon[-\frac{1}{2}, \frac{\sqrt{3}}{2}, 0]$
$a_Q = \frac{a_\epsilon}{2}[0,-1,1]$	$b_L = a_\alpha[1,0,0]$	$c_U = a_\epsilon[0,0,\omega]$
		$c_V = \frac{a_\epsilon}{2}[1, \frac{1}{\sqrt{3}}, \omega]$

are needed to preserve the one-to-one atomic correspondence in a phase transformation function. This is covered in Section 4. Table 2 shows primitive basis vectors in cartesian coordinates considered in this work to generate the motif and lattice of FCC, BCC and HCP crystals. We note that possible differences in the motif – or dimensions – between parent and product phases have not been included in the PTMC or other matrix-based theories, which has caused problems when addressing the crystallography of shear transformations. Differences in N imply that the transformation function cannot be a single 3×3 matrix but additional matrix/vector terms have to be included to consider the changes in crystal symmetry and the face that the transformation function must be at least injective, i.e. map all atoms from the parent onto the product phase. With the new generalised description of a crystal lattice we can proceed to define the necessary functions representing a shear transformation.

3.2. The shear transformation function

Let us consider the parent ($\mathcal{A}$) and product ($\mathcal{B}$) lattices with set of basis vectors $\{a_i\}$ and $\{b_j\}$, respectively, undergo a shear transformation represented by a vector function T. This function is equivalent to the matrix functions used in the Phenomenological Theory of Martensite Crystallography (Eq. (1)), but T is defined to consider dilatation (B) and shear (S) simultaneously and we do not need to pre-define which happens first B or S as in Eq. (5). We first consider the case for $\dim(\mathcal{A}) = \dim(\mathcal{B}) = N$ and the general case is considered in Section 4. If we assume that a phase transformation only involves atomic displacements and no compositional changes then T is linear and injective. This means that, for any lattice point (atom) $A \in \mathcal{A}$ with $A = \sum_{i=0}^{N-1} N_i a_i$, T has the form:

$$T(A) = T\left(\sum_{i=0}^{N-1} N_i a_i\right) = \sum_{i=0}^{N-1} N_i T(a_i) = B. \tag{3}$$

with $B \in \mathcal{B}$. This shows that it is only necessary to calculate T for the basis set $\{a_i\}$ in $\mathcal{A}$, as expected. In addition, we can also see that a_i transforms into a basis vector in $\mathcal{B}$, *i.e.* $T(a_i) = b_k$ with $b_k \in \{b_j\}$. This is because if b_k is not a basis vector in $\mathcal{B}$, it is expressed as $b_k = \sum_{j=0}^{N-1} N_j b_j$ but this would imply that $b_k = T(a_i) = \sum_{j=0}^{N-1} N_j b_j = \sum_{j=0}^{N-1} N_j T(a_j)$ with $a_j \neq a_i$; this means that $a_i = \sum_{j=0}^{N-1} N_j a_j$ but a_i is a basis vector, which represents a contradiction. This relation will be useful when searching all possible combinations of lattice correspondence between the parent and product phase.

Shear and Martensitic transformations involve the collective (shear) displacements of atoms but specific directions remain invariant, which give rise to orientation relationships (ORs) between $\mathcal{A}$ and $\mathcal{B}$. This means that T describes a dilatation along an invariant direction, which is expressed as: if $a_0 \in \mathcal{A}$ is parallel to $b_0 \in \mathcal{B}$ ($a_0 \| b_0$), then $T(a_0) = R(A_0 + \delta\hat{n}_0) = b_0$, where R is an Euclidean rotation matrix, δ is the distortion to match crystal dimensions for $\mathcal{B}$, *i.e.* $\|b_0\|$ and $\hat{n}_0$ is the unit vector for a_0. R is included to rotate the transformed vectors in $\mathcal{B}$ onto the reference coordinate system in $\mathcal{B}$.

Since the shear transformation function consists of transforming an N-dimensional lattice into another N lattice, we need $N-1$ additional functions to represent the phase transformation. The simplest way to represent the remaining functions is to "add" the necessary (shear) displacements, *i.e.* $T(a_i) = R(a_i + s_i) = b_i$ with $i = 1, \dots, N-1$ and s_i is a shear vector $s_i = [x_i, y_i, z_i]$ representing the atomic displacement of atom a_i towards positioning at b_i in $\mathcal{B}$. We will use "shear displacement" throughout the manuscript to differentiate the atomic displacements produced by shear (s_i) to those by dilatation $\delta\hat{n}_0$ during the transformation. Actual (unitless) shears are calculated later in Section 5 to compute the Thermodynamic driving force. We note that a_0 may not be a primitive vector forming the motif, *e.g.* invariant directions in the Greninger–Troiano (GT) Orientation Relationship are not primitive (Table 1), which means that other vectors involved in the transformation function may not be primitive as well. This is further elaborated in Section 4.1.

Combining the previous results the shear transformation function in Eq. (3) is given by:

$$T(A) = R\left(A + N_0\delta\hat{n}_0 + \sum_{j=1}^{N-1} N_j s_j\right) = B, i = 1, \dots, N-1 \tag{4}$$

This equation resembles the form of Eq. (1) for the PTMC but the shear and invariant displacements are represented in terms of specific atomic paths (basis vectors) also highlighting the lack of symmetry in the transformation, therefore addressing items 1 and 3 in Section 2. In addition, the results mathematically show that 2 shear systems are required for the FCC→BCC transformation, therefore explaining why Kelly had to use 2 invariant shear systems for the case of lath martensite. Implications for this and other shear transformations are discussed in the following section. Also, we will discuss about the choice of a_0 and a_i in Section 4. We note that considering invariant parallel directions during a phase transformation is one of the key aspects that identify shear transformations and any predictive model has to incorporate this feature, this assumption is not claimed as a novelty in the present work.

In order to obtain solutions for s_i, we use the geometric relationships for the N primitive vectors in $\mathcal{B}$ to match lattice dimensions and associated symmetries. Assuming $T(A_i) = B_i$, with $A_0 \| B_0$ and A_i, B_i with $i = 1, \dots, N-1$ being linearly independent, we have:

$$\begin{aligned}
\|B_0\| &= \|A_0 + \delta\hat{n}_0\| = \|A_0\| + \delta \\
\|B_i\|^2 &= \left\|A_i + N_{i,0}\delta\hat{n}_0 + \sum_{j=1}^{N-1} N_{i,j}s_j\right\|^2 \\
B_0 \cdot B_i &= \left(A_0 + \delta\hat{n}_0\right) \cdot \left(A_i + N_{i,0}\delta\hat{n}_0 + \sum_{j=1}^{N-1} N_{i,j}s_j\right), i = 1, \dots, N-1 \\
B_1 \cdot B_k &= \left(A_1 + N_{1,0}\delta\hat{n}_0 + \sum_{j=1}^{N-1} N_{1,j}s_j\right) \cdot \left(a_k + N_{k,0}\delta\hat{n}_0 + \sum_{j=1}^{N-1} N_{k,j}s_j\right),
\end{aligned} \tag{5}$$

where $A_i = \sum_{j=1}^{N-1} N_{i,j}a_j$. In addition, we have ignored R in the right hand side of each equation, as vector magnitudes and angles between vectors are preserved under rigid rotations. We note that all vectors are in $\mathbb{R}^3$ and only two angles, *i.e.* projections between 2 vectors via the dot product, are needed. We can easily obtain $\delta = \|B_0\| - \|A_0\|$ from the first equation but solutions for other variables demand more attention. This is because the combination of Eq. (5) gives $3N-3$ non-linear equations (1 for $\|B_0\|$, and $N-1$ for $\|B_i\|$, $B_0 \cdot B_i$ and $B_0 \cdot B_i$) for $3N-2$ unknown variables, δ, x_i, y_i, z_i, which means that Eq. (5) has infinite number of solutions and an additional condition is required to be able to find a finite set solutions to the formulation.

The last equation required for solving the previous system is based on energy principles. Bain first conceived that the martensitic transformation should be such that atomic shift requires minimum motion [40]. Similarly, strain energy minimisation methods have been used to study defect formation at the transformation interface [21] as well as to predict ORs between parent/product phase or matrix/precipitate interfaces [24,41–47]. However, the fact that materials like Fe can undergo multiple shear transformations indicates that there should not only exist one minimum energy configuration but other configurations are possible which could even maximise the strain energy release. To address all possible energy states we employ the Extremum Principle stating that all stationary states, *i.e.* atomic path configurations that are energetically optimal, correspond to the extrema of the transformation strain energy [48]. The Extremum Principle is a well-established Thermodynamic principle that has been used in various applications in Physics and Materials Science involving phase transformations and mechanical stability. For instance, Fischer, et al. [49] provided an overview on the extremum principle applied to Materials Science. Svoboda et al. [50] have used it to predict diffusion-based transformations in metals. Bonvalet-Rolland, et al. [51] have used this concept to model phase nucleation in multicomponent systems. Similarly, several authors have used this principle to derive a comprehensive model for constitutive relations during non-linear plasticity [52–54].

Since the strain energy is proportional to the magnitude of the total shear displacements $\boldsymbol{s}$ [55], the Extrema condition can be written in terms of atomic paths via s_i:

$$\max/\min\{\boldsymbol{s}\} = \max/\min\left\{\sqrt{\sum_i \boldsymbol{s}_i^2}\right\} \tag{6}$$

with $\boldsymbol{s}_i = \|s_i\|$. Eq. (6) is a selection principle for the undetermined system of equations in 5, which allows us to find unique set of solutions for s_i that give the absolute maximum and minimum values from all possible solutions. As for δ, we follow Bain's original argument that δ should be obtained to minimise atomic dilatation; such condition will be necessary for obtaining the ORs in Section 4. It is interesting noting that the solutions for Eq. (5) and $\boldsymbol{s}_i$ form closed curves (covered in the following section). This means that there should be at least 4 extrema energy configurations producing different shear transformations.

In order to illustrate how the theory works, we first consider the FCC→BCC phase transformations in Fe following Kurdjumov–Sachs (KS) and Nishiyama–Wasserman (NW) orientation relationships and later generalise the results in Section 4.

3.3. Case study: FCC→ BCC transformation considering Kurdjumov–Sachs and Nishiyama–Wasserman ORs

Let us consider the primitive vectors for FCC and BCC shown in Table 2. If we first follow Kurdjumov–Sachs (KS) orientation relationship (OR), T involves a dilatation along $\langle 1\bar{1}0\rangle_{FCC}$[1] with parallel $\langle 111\rangle_{BCC}$ direction in BCC. We can consider $a_O \| b_M$ and, for convenience, let us also consider $T(a_P) \to b_N$ and $T(a_Q) \to b_L$, as both sets of vectors are first nearest neighbours of a_O and b_M, respectively. As for Nishiyama–Wasserman OR, $\langle 110\rangle_{FCC} \| \langle 100\rangle_{BCC}$, we consider $a_O \| b_L$, but since b_N is not first nearest neighbour of b_L (Fig. 1b), we need to choose another vector. The extremum principle also dictates that the choice of a_i and b_i should be such that s_i is optimal, therefore, we choose b_2^{NW} =

[1] Vectors in Miller indices are written as $[1\bar{1}0]$ whereas vectors in cartesian coordinates are written in the form $[1,-1,0]$ throughout this manuscript; the former is employed mostly for discussions and the latter is used for the model calculations.

$\frac{a_\alpha}{2}[1,-1,1]$ as it is nearest neighbour of b_L and has same magnitude as other primitive vectors within the BCC unit cell. We therefore have the product basis vectors for the two OR as:

$$\begin{aligned} b_0^{KS} &= \tfrac{a_\alpha}{2}[1,1,1] & b_0^{NW} &= a_\alpha[1,0,0] \\ b_1^{KS} &= a_\alpha[0,0,1] & b_1^{NW} &= \tfrac{a_\alpha}{2}[1,1,1] \\ b_2^{KS} &= a_\alpha[1,0,0] & b_2^{NW} &= \tfrac{a_\alpha}{2}[1,-1,1] \end{aligned} \tag{7}$$

giving the transformation function:

$$\begin{aligned} T(a_O) &= R(a_O + \delta^j \hat{n}_O) = b_0^j \\ T(a_P) &= R(a_P + s_1^j) = b_1^j \\ T(a_Q) &= R(a_Q + s_2^j) = b_2^j \end{aligned} \tag{8}$$

with $s_1^j = [x_1^j, y_1^j, z_1^j]$ and $s_2^j = [x_2^j, y_2^j, z_2^j]$ and $j = KS, NW$. Substituting these values in Eq. (5) we get:

$$\|b_0^j\|^2 = \|a_O + \delta^j \hat{n}_O\|^2 = (\|a_O\| + \delta^j)^2 \|\hat{n}_O\|^2 = (\|a_O\| + \delta^j)^2 \tag{9a}$$

$$\|b_1^j\|^2 = \|a_P + s_1^j\|^2 = \left(x_1^j\right)^2 + \left(\frac{a_\gamma}{2} + y_1^j\right)^2 + \left(\frac{a_\gamma}{2} + z_1^j\right)^2 \tag{9b}$$

$$\|b_2^j\|^2 = \|a_Q + s_2^j\|^2 = \left(\frac{a_\gamma}{2} + x_2^j\right)^2 + \left(y_2^j\right)^2 + \left(\frac{a_\gamma}{2} + z_2^j\right)^2 \tag{9c}$$

$$b_0^j \cdot b_1^j = (a_O + \delta^j \hat{n}_O) \cdot (a_P + s_1^j) = \frac{(\frac{a_\gamma}{\sqrt{2}} + \delta^j)}{\sqrt{2}} \left(x_1^j - y_1^j + \frac{a_\gamma}{2}\right) \tag{9d}$$

$$b_0^j \cdot b_2^j = (a_O + \delta^j \hat{n}_O) \cdot (a_Q + s_2^j) = \frac{(\frac{a_\gamma}{\sqrt{2}} + \delta^j)}{\sqrt{2}} \left(x_2^j - y_2^j + \frac{a_\gamma}{2}\right) \tag{9e}$$

$$\begin{aligned} b_1^j \cdot b_2^j = (a_P + s_1^j) \cdot (a_Q + s_2^j) = x_1^j \left(\frac{a_\gamma}{2} + x_2^j\right) + \left(\frac{a_\gamma}{2} + y_1^j\right) y_2^j \\ + \left(\frac{a_\gamma}{2} + z_1^j\right)\left(\frac{a_\gamma}{2} + z_2^j\right) \end{aligned} \tag{9f}$$

where we can easily obtain $\delta^{KS} = \frac{\sqrt{3}a_\alpha}{2} - \frac{a_\gamma}{\sqrt{2}}$ and $\delta^{NW} = a_\alpha - \frac{a_\gamma}{\sqrt{2}}$. It is interesting to highlight that the equations for KS and NW only differ by 4 constant values, *i.e.* $\|b_0^j\|$, $\|b_1^j\|$, $\|b_2^j\|$ and $b_1^j \cdot b_2^j$. This suggests that solutions for KS and NW have similar behaviour, which is consistent with experimental and theoretical observations reporting that these ORs are the most commonly reported in Fe [10,28]. As for the shape of the solutions, for this particular choice of vectors, y_1^j and y_2^j are linearly related to x_1^j and x_2^j, respectively, with slope equal to −1 (Eq. (9)d and (e). This means that the rate change for shear displacements s_1^j and s_2^j is equal along a_O ($[1\bar{1}0]$). As for z_1^j and z_2^j, two solutions exist in each case given the quadratic form of Eq. (9)b and c. Finally, Eq. (9)f shows that s_1^j and s_2^j are non-linearly related to each other indicating that one vector variable can be solved first, *e.g.* s_1, to later determine the other. To better understand the physical meaning of possible solutions for s_1^j and s_2^j, we can also compute their associated habit planes by calculating the normal vector to s_i and a_O (invariant direction):

$$\begin{aligned} HP_1^j &= \frac{a_O \times s_1^j}{\|a_O \times s_1^j\|} \\ HP_2^j &= \frac{a_O \times s_2^j}{\|a_O \times s_2^j\|} \end{aligned} \tag{10}$$

Geometrically, this formula calculates the planes (via their normal vectors) formed by the invariant direction and shear directions, *i.e.* these planes define the directions not affected by s_1 and s_2.

We present an algorithm to calculate the (cartesian) habit planes in (integer) Miller indices. We first note that the Miller indices of a plane are computed as the intersection of the plane with the 3 axes (for a cubic lattice). We can use the equation of a plane to find such intersections: $HP_i^j \cdot \bar{r} = A$, where $HP_i^j = (HP_{i,x}^j, HP_{i,y}^j, HP_{i,z}^j)$ is the normal vector to the habit plane (Eq. (10)), $\bar{r} = (x, y, z)$ is any point on the plane, and A is a constant. We also note that the habit plane calculated in Eq. (10) includes the origin, which would make $A = 0$ as $\bar{r} = (0,0,0)$ is on the plane and we therefore cannot compute the Miller Indices. Instead, we consider an adjacent plane with same orientation, *i.e.* same normal vector, that does not contain the origin such that $A \neq 0$ to give the equation: $HP_{i,x}^j x + HP_{i,y}^j y + HP_{i,z}^j z = A$. We also highlight that HP_i^j are of the form $(l\ l\ k)$, as these vectors are orthogonal to a_O (see Eq. (10)), which means that $HP_{i,x}^j = HP_{i,y}^j$. We can now compute the intersections with the 3 axes. Considering the case of $z = y = 0$, we find that $A = HP_{i,x}^j N_{MI}$ with N_{MI} being a normalising constant to make Miller indices integers (or close to). An identical solution is obtained when $z = x = 0$. Lastly, when $x = y = 0$, the z_{MI} component equals to $HP_{i,z}^j z_{MI} = HP_{i,x}^j N_{MI}$ or $z_{MI} = \frac{HP_{i,x}^j}{HP_{i,z}^j} N_{MI}$. This gives the equivalent habit plane in Miller indices as:

$$\begin{aligned} HP_1^j(\text{Miller}) &= N_{MI}\left(1\ 1\ \frac{HP_{1,x}^j}{HP_{1,z}^j}\right) \\ HP_2^j(\text{Miller}) &= N_{MI}\left(1\ 1\ \frac{HP_{2,x}^j}{HP_{2,z}^j}\right) \end{aligned} \tag{11}$$

N_{MI} is adjusted to produce the closest combination of vectors having integer components according to experimental reports. This equation is also useful to transform the habit planes in Miller index notation back to cartesian coordinates in the form of Eq. (10).

We note that 2 habit planes are calculated given that, mathematically, two solutions (plus the solution to the invariant direction) are needed to make the transformation injective. Eq. (9) have been solved numerically to study the behaviour of the solutions for $\boldsymbol{s_1^j} = \|s_1^j\|$, $\boldsymbol{s_2^j} = \|s_2^j\|$ and $\boldsymbol{s}^j$ in each OR case. Solutions were numerically found by assigning specific values to a variable, *i.e.* x_1^j for simplicity, and solving the equations for the remaining variables using Newton–Raphson integration. The lattice parameters of Fe were used for the calculations: $a_\gamma = 0.385$ nm and $a_\alpha = 0.286$ nm. Figs. 2(a) and (b) show the results for $\boldsymbol{s_1^j}$ (solid lines) and $\boldsymbol{s_2^j}$ (dashed lines) for KS and NW, respectively. The two sets of solutions for $\boldsymbol{s_2^j}$ are represented by the pink and purple lines, respectively. Each set of solutions represent a closed curve with 4 extrema, one minimum and maximum for y_1^j as well as a minimum and maximum for $\boldsymbol{s_1^j}$; the meaning of the 4 extrema is discussed below. For the case of KS OR, solutions for s_2^{KS} are not symmetric, whereas for NW they are antisymmetric about $y_1^{KS} \sim 0.10$ nm. Fig. 2(c) shows results for $\boldsymbol{s}^j = \sqrt{(\boldsymbol{s_1^j})^2 + (\boldsymbol{s_2^j})^2}$ following the two possible solutions for KS. $\boldsymbol{s}^{KS}$ for the second solution (pink line) has values greater than a_γ indicating that the total shear displacements are always greater than the unit cell, *i.e.* atoms will likely move more than 1 unit cell in length, hence the purple solution is considered to be the correct one. Fig. 2(d) compares $\boldsymbol{s}$ between KS and NW confirming that they are very similar.

Although there are multiple combined extrema for $\boldsymbol{s_1}$ and $\boldsymbol{s_2}$, $\boldsymbol{s}$ has only 4 extrema regardless of the OR, *i.e.* there is one absolute minimum ($\boldsymbol{s}^{bain}$) and maximum ($\boldsymbol{s}^{plate}$) for x_1 and one minimum ($\boldsymbol{s}^{lath}$) and maximum ($\boldsymbol{s}^{lent}$) for the total shear $\mathbf{s}$. These 4 solutions are particularly important as, from a Thermodynamic standpoint, they represent the conditions of maximum and minimum energy release due to shear displacements, as the driving force is proportional to $\boldsymbol{s}^2$. This will be addressed in Section 5. Solutions leading to $\boldsymbol{s}^{lath}$ and $\boldsymbol{s}^{plate}$ are those where $\boldsymbol{s}$ produces the minimum and maximum atomic displacements, respectively. $\boldsymbol{s}^{lath}$ and $\boldsymbol{s}^{plate}$ can be interpreted as the solutions occurring when there is no other driving force for the phase transformation and atomic distortions resulting from the transformation must be entirely accommodated by shear displacements. Conversely, $\boldsymbol{s}^{bain}$ are the solutions with the minimum shear which occur if there is another mechanism promoting atomic displacements, such as diffusion. We note that numerical values for $\boldsymbol{s}$ do not change if solutions are chosen for a different variable than x_1. It is also interesting to note that solutions for s_i are never zero. This means that 2 shear functions are required to mathematically solve the (injective) transformation function

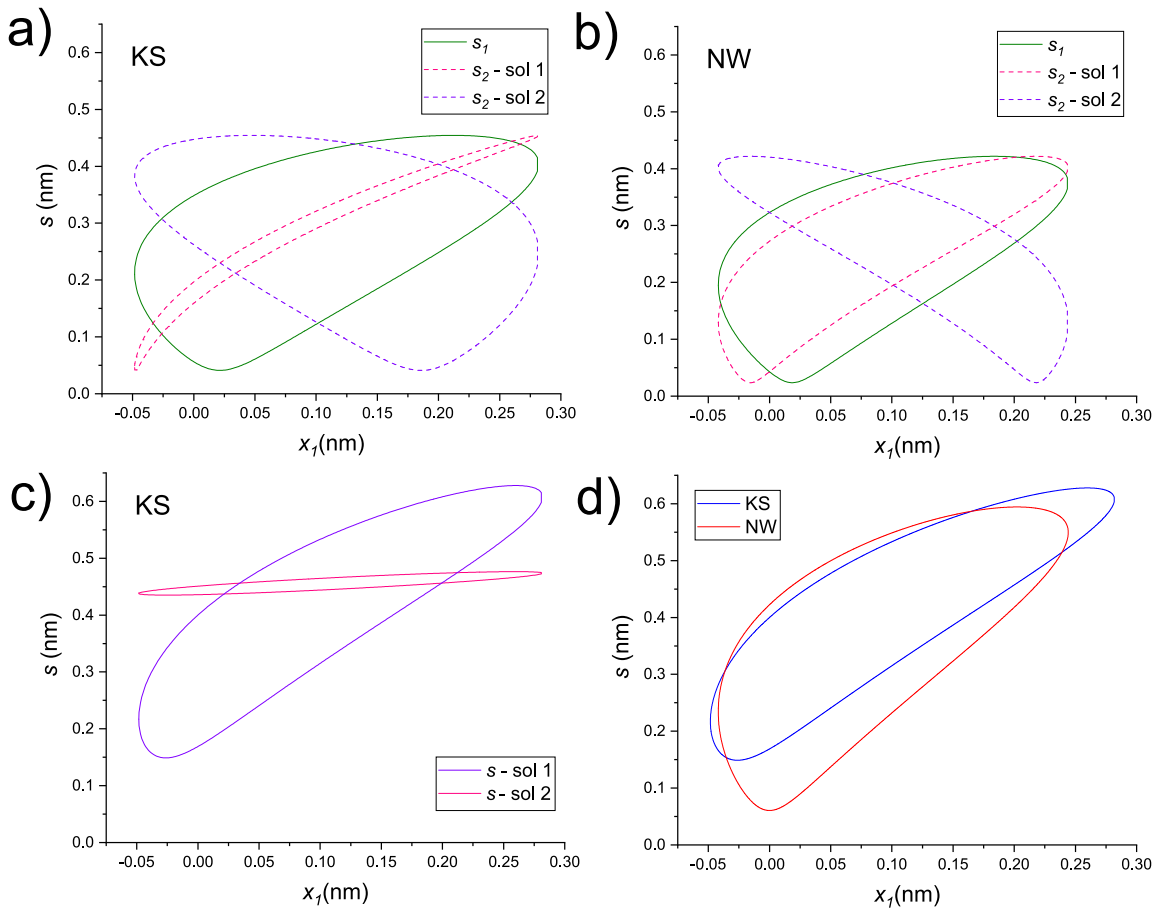

Fig. 2. Individual shear displacements, s_1 and s_2, for (a) KS and (b) NW ORs. (c) Possible solutions for total displacement $\boldsymbol{s}$ for KS and (d) comparison in $\boldsymbol{s}$ between KS and NW.

of FCC→BCC crystals, justifying why Kelly had to use the double shear model for lath martensite. Discussion of why only one shear can be used in twinned martensite is presented in Section 5.1. The extremum principle dictates that the extrema are the only possible "equilibrium" solutions. Let us now explore the predicted shear displacements s_i and habit planes at the 4 extrema in order to understand the meaning of the solutions obtained.

To validate our predictions we use experimental and theoretical results from classical and modern works that have been subject of multiple discussions [2,19,26,29,56–58] and which the community widely acknowledges as the primary crystallographic features, crystal defects forming, and Thermodynamic driving force of specific shear transformations in Fe [1,2]. Table 3 shows values for $\boldsymbol{s}^j$, individual shear displacements s_1^j and s_2^j (in cartesian coordinates) and their respective habit planes at the 4 extrema; the first and second row in each OR represents values for s_1 and s_2, respectively. To better illustrate the atomic mechanisms predicted, Fig. 3 shows schematics of the associated atomic displacement of the extrema following KS OR projected onto the $(110)_{FCC}$ plane; atomic mechanisms for NW are similar and are not shown for simplicity in the discussion. The orange atoms represent the initial positions of a_O, a_P and a_Q and the green atoms represent their final position after the transformation (relative to the FCC system), noting that $\tilde{b}_1 = a_1 + s_1 = R^{-1}b_1$ and $\tilde{b}_2 = a_2 + s_2 = R^{-1}b_2$; similarly, arrows represent the direction of s_1 and s_2.

For $\boldsymbol{s}^{bain}$, s_1^{bain} and s_2^{bain} are orthogonal in the xy plane (or almost orthogonal for NW), showing small symmetric displacements that "open" the FCC lattice into the BCC lattice (Fig. 3a). The shear magnitude, direction and habit planes for KS are very close to the values reported for Widmanstätten Ferrite. Watson and McDougall [56] calculated the average values for Widmanstätten Ferrite plates using the PTMC to be approximately $\boldsymbol{s} = 0.36a_\gamma = 0.129$ nm, $s = [-0.11, 0.053, 0.0357]$ and $HP = (0.5057, 0.4523, 0.7346)$ (in cartesian coordinates). The agreement is remarkable, apart from the ordering in the vector components. Moreover, the symmetry between HP_1^{bain} and HP_2^{bain} is also consistent with the fact that the formation of Widmanstätten Ferrite involves the simultaneous growth of two plates, which are crystallographic variants such that their shape deformations accommodate mutually; other authors have found similar ratios in the habit planes of Widmanstätten Ferrite [59]. Widmanstätten Ferrite has been observed in low carbon lean steels [60,61] and in interstitial-free Fe–Ni alloys and meteorites [62] under very slow cooling; this is because the structures require very low undercooling [1,63], *i.e.* small shear displacement, but take a long time to nucleate. Interestingly, for the NW results, the predicted habit planes are close to $(223)_{FCC}$ –or (0.663,0.659,0.373) in cartesian coordinates– consistent with habit planes of individual sub-units measured for Bainite [2]. Therefore, the model suggests $\boldsymbol{s}^{bain}$ covers the transformation mechanisms associated to Widmanstätten structures and Bainite, and these form as the configurations requiring the lowest shear displacements or smallest atomic paths. Further evidence is presented in the following section on how to differentiate them.

The results for $\boldsymbol{s}^{lath}$ show that shear is not symmetric, as s_1^{lath} has much greater magnitude than s_2^{lath}. Interestingly, Fig. 3b illustrates the resulting vector for $\tilde{b}_1$ lying on the xy plane and s^{lath} involving atomic shifting by 1 layer. The four habit planes predicted for s^{lath} (in Miller indices) are $(\bar{1}\ 1\ 0.85)_{FCC}$, $(5\ \bar{5}\ 7.1)_{FCC}$, and $(\bar{1}\ \bar{1}\ 1.7)_{FCC}$ and $(1\ \bar{1}\ 0.12)_{FCC}$, which are very close to the habit planes reported for lath martensite, most notably those close to $\{5\ 5\ 7\}_{FCC}$ [29,64], but also $(1\ 1\ 1.7)_{FCC}$ [26] and $(1\ 1\ 1)_{FCC}$ [58]. Moreover, for the KS OR case, the values of $s_1^{lath} \approx \frac{a_\gamma}{2}[0.56\ 0.26\ \bar{1}]$ with $HP_1^{lath} \approx (\bar{1}\ 1\ 0.85)$ are

Table 3
Shear displacement and respective habit planes of the 4 extrema for **s** in cartesian and Miller notation.

OR	$\boldsymbol{s}^{bain}$ (nm)	s_i^{bain} (nm)	HP_i^{bain} (Cart)	HP_i^{bain} (Miller)
KS	0.149	[0.081,0.026,−0.063]	(0.451,0.451,0.769)	(8.5 8.5 5)
		[−0.026,−0.08,−0.061]	(0.446,0.446,0.775)	(8.6 8.6 $\bar{5}$)
NW	0.06	[0.026,0.003,−0.041]	(0.642,0.642,0.42)	(5 5 7.64)
		[0.003,−0.019,−0.03]	(0.644,0.644,−0.41)	(5 5 $\overline{7.85}$)
OR	$\boldsymbol{s}^{lath}$ (nm)	s_i^{lath} (nm)	HP_i^{lath} (Cart)	HP_i^{lath} (Miller)
KS	0.217	[0.10,0.047,−0.179]	(0.6,0.6,0.51)	(1 1 1.17)
		[0.034,−0.02,0.022]	(−0.63,−0.63,0.44)	($\bar{5}$ $\bar{5}$ 7.15)
NW	0.234	[0.064,0.041,−0.179]	(0.65,0.65,0.38)	(5 5 8.5)
		[0.101,0.077,0.0219]	(0.12,0.12,−0.98)	(1 1 $\overline{0.1}$)
OR	$\boldsymbol{s}^{plate}$ (nm)	s_i^{plate} (nm)	HP_i^{plate} (Cart)	HP_i^{plate} (Miller)
KS	0.63	[−0.204,−0.259,−0.296]	(0.474,0.474,−0.741)	(3 3 $\bar{2}$)
		[0.26,0.205,−0.294]	(0.474,0.474,0.745)	(3 3 2)
NW	0.59	[−0.178,−0.202,−0.322]	(0.54,0.54,−0.64)	(1 1 $\overline{0.84}$)
		[0.202,0.179,−0.321]	(0.54,0.54,0.64)	(1 1 0.84)
OR	$\boldsymbol{s}^{lent}$ (nm)	s_i^{lent} (nm)	HP_i^{lent} (Cart)	HP_i^{lent} (Miller)
KS	0.59	[−0.22,−0.28,−0.179]	(−0.316,−0.316,0.895)	($\overline{5.6}$ $\overline{5.6}$ 2)
		[0.199,0.144,−0.38]	(−0.596,−0.596,−0.538)	($\bar{1}$ $\bar{1}$ $\overline{1.1}$)
NW	0.54	[−0.22,−0.243,−0.179]	(−0.33,−0.33,0.87)	($\overline{5.2}$ $\overline{5.2}$ 2)
		[0.101,0.077,−0.38]	(−0.67,−0.67,−0.31)	($\bar{1}$ $\bar{1}$ $\bar{2}$)

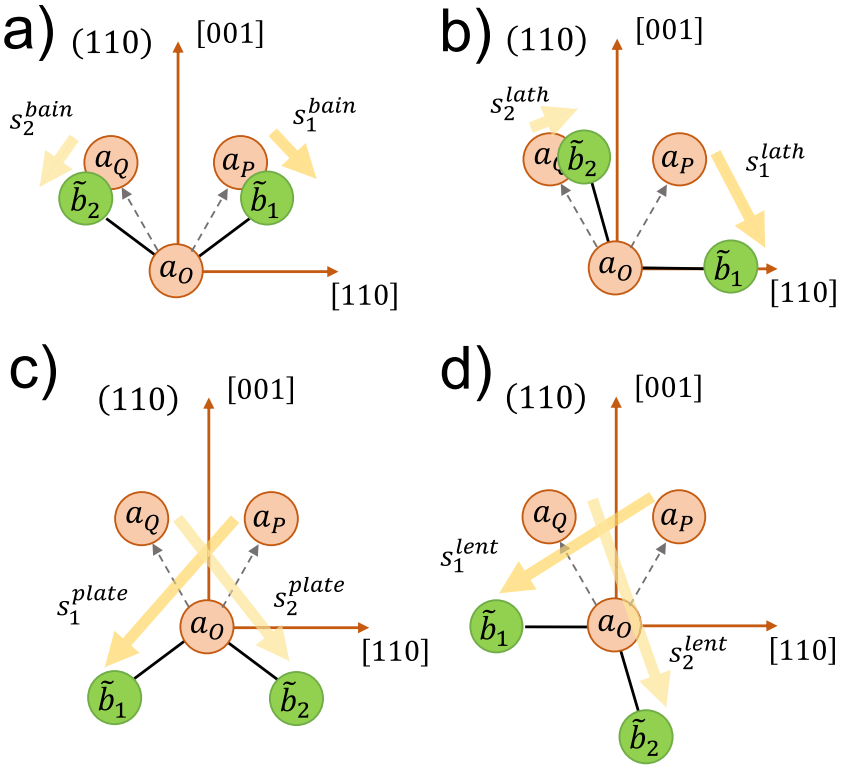

Fig. 3. Atomic paths of extrema obtained for KS OR projected onto $(110)_{FCC}$: (a) minimum shear, (b) minimum displacements, (c) maximum shear, and (d) maximum displacements.

close to the Burgers vector of a $\frac{1}{2}[10\bar{1}]$ dislocation forming in a $(\bar{1}\ 1\ 1)_{FCC}$ plane. Experimentally, it has been determined that the FCC/BCC interface of lath martensite is stepped following $(111)_{FCC}\|(011)_{BCC}$ with step direction close to $\frac{1}{2}[\bar{1}01]_{FCC}$[26]. Interfacial defects form as the interface orientation (habit plane) is misoriented 10° and 20° about $\frac{1}{2}[1\bar{1}0]_{FCC}$, *i.e.* lying between (557) and (112). The Burgers vector of these defects is $\sim \frac{1}{2}[\bar{1}01]_{FCC}$ (or $\sim \frac{1}{2}[1\bar{1}1]_{BCC}$) and the model successfully recovers this structure. In addition, the normalised shear direction $\hat{s}_1^{lath} = \frac{s_1^{lath}}{\|s_1^{lath}\|} = [0.47, 0.22, -0.85]$ is close to the second shear direction obtained by Kelly [29] using the PTMC $\hat{s} = [0, 0.81, -0.58]_{FCC}$, although for different slip direction. s_2^{lath} for KS OR represents a small "dilatation" along $\sim [1\bar{1}1]_{KS}$. Values of s_1^{lath} for NW case follow similar trends but to lesser extent and s_2^{lath} represents a small "dilatation" along $\sim [110]_{FCC}$. Therefore, the present model predicts that the mechanisms associated to $\boldsymbol{s}^{lath}$ corresponds to lath martensite, *i.e.* diffusionless lath martensite forms as the shear configuration minimising atomic displacements when there is no other driving force. In addition it has been shown that $\frac{1}{2}[10\bar{1}]$ dislocations form, via s_1^{lath}, simultaneously as the phase transformation takes place.

For the case of $\boldsymbol{s}^{plate}$ and $\boldsymbol{s}^{lent}$, these values are greater than a_γ indicating that atomic displacements are more pronounced in these configurations. Figs. 3(c) and (d) depict similar symmetric and asymmetric atomic displacements, as with $\boldsymbol{s}^{bain}$ and $\boldsymbol{s}^{lath}$, respectively, but atomic paths now resemble twinning mechanisms about $[1\bar{1}0]_{FCC}$, consistent with plate and lenticular martensite structures. The main difference

between plate and lenticular martensite is that plate martensite forms as fine structures ($\lesssim$ 1 μm in thickness) containing nano-sized twins, whereas plates are coarser ($\gtrsim$ 1 μm in thickness) in lenticular martensite but they also contain a high density of tangled dislocations outside the twinned regions (midrib) [65]; lenticular martensite forms at higher temperatures than plate martensite [66]. The occurrence of twinning is easily seen when calculating individual shear displacements. For KS OR case we have $s_1^{lent} = \frac{a_\gamma}{2}[-1.2,-1.56,-1]$, $s_2^{lent} = \frac{a_\gamma}{2}[1.1,0.8,-2.1]$, $s_1^{plate} = \frac{a_\gamma}{2}[-1.1,-1.44,-1.65]$ and $s_2^{plate} = \frac{a_\gamma}{2}[1.45,1.14,-1.64]$, whereas for NW OR shear displacements are $s_1^{lent} = \frac{a_\gamma}{2}[-1.22,-1.35,-1]$, $s_2^{lent} = \frac{a_\gamma}{2}[-0.56,-0.4,-2.1]$, $s_1^{plate} = \frac{a_\gamma}{2}[-0.99,-1.12,-1.79]$ and $s_2^{plate} = \frac{a_\gamma}{2}[1.12,1,-1.79]$. All cases represent $\sim \frac{a_\gamma}{2}\langle 211\rangle$ twinning systems in the FCC lattice. Moreover, on a closer look to s_i, one can see that all solutions are of the form:

$$
\begin{aligned}
s_1^{plate,KS} &= \frac{a_\gamma}{2}[\bar{1},\bar{1},\bar{2}] - [0.02,0.08,-0.062] = \frac{a_\gamma}{2}[\bar{1},\bar{1},\bar{2}] - \tilde{s}_1^{bain,KS}\\
s_2^{plate,KS} &= \frac{a_\gamma}{2}[1,1,\bar{2}] - [-0.08,-0.026,-0.064] = \frac{a_\gamma}{2}[1,1,\bar{2}] - \tilde{s}_2^{bain,KS}\\
s_1^{plate,NW} &= \frac{a_\gamma}{2}[\bar{1},\bar{1},\bar{2}] - [0,0.02,-0.036] = \frac{a_\gamma}{2}[\bar{1},\bar{1},\bar{2}] - \tilde{s}_1^{bain,NW}\\
s_2^{plate,NW} &= \frac{a_\gamma}{2}[1,1,\bar{2}] - [-0.023,0,-0.037] = \frac{a_\gamma}{2}[1,1,\bar{2}] - \tilde{s}_2^{bain,NW}\\
s_1^{lent,KS} &= \frac{a_\gamma}{2}[\bar{1},\bar{1},\bar{2}] - [0.04,0.1,-0.179] = \frac{a_\gamma}{2}[\bar{1},\bar{1},\bar{2}] - \tilde{s}_1^{lath,KS}\\
s_2^{lent,KS} &= \frac{a_\gamma}{2}[1,1,\bar{2}] - [-0.02,0.035,0.022] = \frac{a_\gamma}{2}[1,1,\bar{2}] - \tilde{s}_2^{lath,KS}\\
s_1^{lent,NW} &= \frac{a_\gamma}{2}[\bar{1},\bar{1},\bar{2}] - [0.04,0.06,-0.179] = \frac{a_\gamma}{2}[\bar{1},\bar{1},\bar{2}] - \tilde{s}_1^{lath,NW}\\
s_2^{lent,NW} &= \frac{a_\gamma}{2}[1,1,\bar{2}] - [0.078,0.1,0.022] = \frac{a_\gamma}{2}[1,1,\bar{2}] - \tilde{s}_2^{lath,NW}
\end{aligned}
\tag{12}
$$

with $\tilde{s}_i^{k,j}$, $i = 1,2$, $j = KS, NW$ and $k = bain, lath$ being vectors representing excess strains with almost identical magnitude and direction to their untwinned counterparts, *i.e.* $s_i^{k,j}$, but with swapped x and y components to match the inverse invariant direction promoted by twinning (Table 3). A physical interpretation of this result is that in $\boldsymbol{s}^{plate,j}$ twinning accommodates more effectively the transformation strain as their magnitude is closer to the shear of single twins, whereas $s_i^{lent,j}$ are lower than those for twinning and additional shear mechanisms are necessary to balance the excess distortions from the twinning process. The results also indicate that twinning occurs in pairs and that the "interface" plane forming between these variants is $(110)_{FCC}$, consistent with other works [19]; the results could help in further explaining why twin variant-pairing occurs in plate/lenticular martensite but further work is needed to expand on the predictions [67]. This analysis is consistent with the mechanisms of plate and lenticular martensite formation sequence [68]: Nano/micro twinning marks the start of the transformation to accommodate the lattice strains in plate martensite and, for lenticular martensite, twinning is followed by the formation a high density of tangled dislocations outside the twinned regions to accommodate the excess strains ($\tilde{s}_i^{k,j}$) [69]. As for the habit planes, HP_2^{lent} in NW OR is close to the reported habit plane for twinned martensites [70]: $\{\bar{2}\,\bar{2}\,\bar{5}\}$ –or (−0.68,−0.68,−0.27) in cartesian coordinates–. HP_2^{lent} for KS OR is close to (111). As for HP_1^{lent} in both ORs it is about 7.76° from {15 10 3}, another habit plane reported in plate and lenticular martensite [71]; this habit plane will be revisited in the next section when addressing the predictions for Greninger–Troiano OR. The results indicate that the atomic mechanisms associated to $\boldsymbol{s}^{lent}$ and $\boldsymbol{s}^{plate}$ correspond to lenticular and plate martensite structures, respectively, where twinning is the dominant shear accommodation mechanism. As with the case of lath martensite, the model predicts that twinning, additional atomic shear displacements and the phase transition occur simultaneously.

We highlight that although the predicted atomic displacements of 0.2–0.6 nm – or 2-6 Angstrom – for $\boldsymbol{s}_i^{k,j}$ may seem large, they are realistic and consistent with experimental evidence, via crystal defects observed in martensite. Large displacements can happen when (elastic) deformation twinning forces atoms to mirror their planes relative to their initial position. We have shown that the large predicted displacements for $\boldsymbol{s}^{plate}$ and $\boldsymbol{s}^{lent}$ correspond to ⟨112⟩ twins – with magnitude of atom displacements equal to $\sqrt{\frac{3}{2}}a_\gamma = 4.38$ Å– plus smaller displacements ($\lesssim$ 1.3 Å). Similarly, the atomic displacements caused by a ⟨110⟩ dislocation in the FCC lattice is 0.25 nm = 2.5 Å, a value consistent with $\boldsymbol{s}^{lath}$. The analysis in this section has been made only for a single set of vectors for FCC and 2 for BCC under the assumptions that either KS or NW ORs operate. However there is nothing in the analysis restricting the choice of vectors in the parent and product phases and many more atomic configuration can exist with different vector choices, including variants of the same OR. In addition, other ORs could exist in addition to the known ORs in FCC→BCC with associated variants (Table 1). Results of the theory are generalised in the next section to cover for all possible configurations leading to specific orientation relationships and the calculation of shear displacements of all possible variants. To do this, we will first identify possible invariant directions at the parent and product phases, *i.e.* a_0 and b_0 predicting specific ORs, to later identify complementing basis vectors defining the corresponding parallel plane conditions and associated shear displacement functions.

4. Model generalisation: Predicting orientation relationships and total shear displacement functions

So far, no specific consideration has been given about the choice of B_0 and A_0 in the derivation and in Eq. (4) but these vectors give rise to the underlying orientation relationships in the transformation vector function. Although B_0 and A_0 in Section 3.3 were chosen to satisfy specific variants of KS or NW ORs, there are many more vector combinations towards defining T for other variants in KS and NW ORs as well as representing other valid ORs. This implies that a criterion for which ORs are feasible in a given transformation function is needed. In addition, the treatment of the crystal lattice and shear transformation functions in previous sections was defined considering atoms as 1D lattice points but in reality, both dilatation and shear displacement functions, should be defined such that they do not interfere with the atomic packing sequence of the parent and product lattices. The most convenient way to address this requirement is to consider atoms as hard-spheres, as proposed by other authors [18,72,73]. The first step is to identify suitable vector pairs for A_0 and B_0 and later find the missing basis vectors to be able to define T.

For the dilatation function, lattice distortions should respect the hard sphere packing of atoms and this geometric consideration requires that the distance of A_0 to its first nearest neighbour (1NN) must be greater than an atomic radius distance, *i.e.* the radius of a hard-sphere. This is because dilatation may be impeded if a nearby atom is close enough to prevent atomic displacement along A_0. Fig. 4 shows a schematic of this mechanism. Although δ may be very small, since T spans across the entire lattice, there is a lattice point of the form $N_\delta A_0$ with $N_\delta \in \mathbb{N}$ such that $N_\delta \delta \hat{n}_0$ is large enough to interfere with its 1NN. Therefore, we have to introduce a dilatation criterion where the directions of a parent lattice can only be invariant, *i.e.* dilatation directions, if the distance to their 1NN is greater than r_a:

$$
d_{1NN} = \min(\|A_k - (A_k \cdot \hat{n}_{A_0})\hat{n}_{A_0}\|) > r_a \text{ for } A_k \in \mathcal{A} \tag{13}
$$

where $\hat{n}_{A_0} = A_0/\|A_0\|$. Experimentally, ORs are typically observed to be matching directions on close-packed planes, which may be attributed to correlated evolution at the interface [74]. Such observation has been used in previous models to predict ORs between matrix and precipitates, such as the edge-to-edge matching model [75]. This is because energy minimisation occurs when close-packed rows of atoms match across the interface, as in the present case. Following the previous arguments, we assume in the first instance that combinations of A_0 and B_0 leading to invariant directions are only given by directions lying on close-packed planes of the respective lattice and with A_0 satisfying

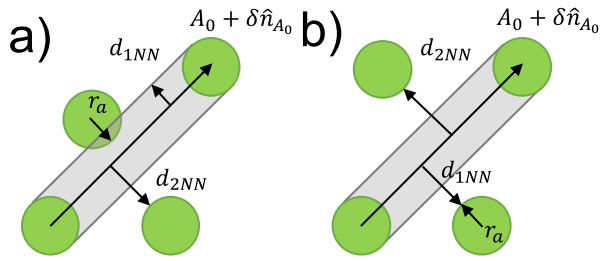

Fig. 4. Hard-sphere model indicating possible (a) obstruction and (b) clearance from 1NN when undergoing dilatation along A_0.

Table 4
Lattice distortion calculations for various combinations of invariant directions following the minimum dilatation criterion.

FCC	BCC	δ (nm)	Candidate ORs
$\frac{1}{2}\langle 110\rangle$	$\frac{1}{2}\langle 111\rangle$	−0.005	KS, P
$\frac{1}{2}\langle 110\rangle$	$\langle 100\rangle$	0.0328	NW
$\frac{1}{2}\langle 110\rangle$	$\langle 110\rangle$	0.15	–
$\frac{1}{2}\langle 211\rangle$	$\langle 100\rangle$	−0.19	–
$\frac{1}{2}\langle 211\rangle$	$\frac{1}{2}\langle 111\rangle$	−0.15	–
$\frac{1}{2}\langle 211\rangle$	$\langle 100\rangle$	−0.033	GT
BCC	HCP	δ (nm)	Candidate ORs
$\frac{1}{2}\langle 111\rangle$	$\langle 11\bar{2}0\rangle$	−0.0063	B, P
$\langle 100\rangle$	$\langle 11\bar{2}0\rangle$	−0.032	PS, RD
FCC	HCP	δ (nm)	Candidate ORs
$\langle 110\rangle$	$\langle 11\bar{2}0\rangle$	0.00085	SN
$\frac{1}{2}\langle 211\rangle$	$\langle 11\bar{2}0\rangle$	−0.18	–

Eq. (13). Further analysis could be done in future work to explore if this assumption can be relaxed to find new ORs on non close-packed planes.

Fig. 5 shows normalised contour plots (d_{1NN}/r_a) for the (a) FCC, (b) BCC and (c) HCP crystal lattices in Fe. Only dilatation can occur if $d_{1NN}/r_a \geq 1$ with $r_a = 0.126$ nm. The plots have been obtained by first assigning a dilatation direction A_0 and calculating the 1NN distance using Eq. (13). This process was done for every lattice direction on $(111)_{FCC}$, $(101)_{BCC}$ and $(0001)_{HCP}$ up to vector radii of about $7a_\gamma$, $8.6a_\alpha$ and $10a_\epsilon$, respectively. Similar calculations were done on other closed packed planes showing very similar results. For the FCC case, only the twelve $\frac{1}{2}\langle 110\rangle_{FCC}$ ($d_{1NN}/r_a = 1.74$) and twelve $\frac{1}{2}\langle 211\rangle_{FCC}$ ($d_{1NN}/r_a = 1.004$) directions satisfy this criterion; the closest set of directions with higher computed distance were $\langle 311\rangle_{FCC}$ with $d_{1NN}/r_a = 0.657$. Similarly for the BCC case, only the six $\langle 100\rangle_{BCC}$ and six $\frac{1}{2}\langle 111\rangle_{BCC}$ directions satisfy Eq. (13); the next highest value for this crystal structure is $\langle 110\rangle_{BCC}$ with $d_{1NN}/r_a = 0.96$ ($y = \pm 3x$ directions in the plot). As for the HCP lattice, only the two $\langle 11\bar{2}0\rangle_{HCP}$ and four $\langle 10\bar{1}0\rangle_{HCP}$ directions satisfy the previous criterion; the next set is for $\langle 12\bar{3}0\rangle_{HCP}$ with $d_{1NN}/r_a = 0.99$ ([0,0,1] and $y = \pm\frac{1}{2}x$ directions in the plot). Similar results were obtained when considering Ti with $r_a = 0.147$ nm. The results indicate that, under the present assumptions, the invariant directions for FCC, BCC, and HCP as parent phases, *i.e.* A_0, correspond to $\langle 110\rangle_{FCC}$, $\langle 211\rangle_{FCC}$, $\langle 100\rangle_{BCC}$, $\frac{1}{2}\langle 111\rangle_{BCC}$ and $\langle 11\bar{2}0\rangle_{HCP}$ directions, all consistent with experimentally reported ORs in several materials [76–78].

As for the invariant directions matching the product phase B_0, previous works [35] have shown that KS and NW are prolific ORs in FCC→BCC as their associated directions induce the lowest distortions during the transformation. This implies that the invariant direction for the product phase (B_0) has to be such that the dilatation $\delta = \|B_0\| - \|A_0\|$ is small, at least lower than r_a, as with the 1NN criterion. Table 4 shows the calculations for different direction combinations for FCC→BCC, BCC→HCP and FCC→HCP transitions in Fe and respective candidate ORs. For the product phases, vector directions within the unit cell are only considered as these contain the directions with the lowest length. B, P, PS, RD and SN stand for Burgers, Potter, Pitsch–Scharder, Rong–Dunlop and Shoji–Nishiyama orientation relations [77,78]. The results imply that commonly observed ORs involve direction combinations with the lowest dilatation, although other ORs may be present. The predictions for FCC→BCC case are further developed in the following sections. The novelty of this section is that it has been possible to (partially) predict the reported ORs between FCC, BCC and HCP crystals using the same vector function approach and the assumptions made in this Section are consistent with similar Matrix-based approaches. The only missing part is to identify the variants involved in each OR in order to identify parallel planes and fully predict the ORs and the associated shear distortions per variant.

4.1. Calculating shear displacements to predict ORs

The next step is to identify the remaining sets of vectors $\{A_i\}$ and $\{B_i\}$ ($i = 1, \ldots, N-1$) -for a predefined set of invariant directions A_0 and B_0- and find all possible vector combinations for T that lead to different transformation variants. Based on the initial requirement of a primitive cell spanning the lattice, the choice of $\{A_i\}$ and $\{B_i\}$ has to be such that their magnitude is as low as possible. Also, the energy minimisation principle requires that at least some of these are 1NNs to A_0 to induce the lowest shear displacements but other linearly independent vectors could be second nearest neighbours (2NN). This is because 1NN vectors may lie on the same plane as A_0 and its 1NN therefore not being able to span the lattice. For example, in the FCC→BCC case studied in Section 3.3, a_P and a_Q are 1NN to a_O and lie on different planes, *i.e.* a_P and a_Q lie on the $(11\bar{1})_{FCC}$ and $(111)_{FCC}$ planes, respectively, but the vector $\frac{a_\gamma}{2}[0\bar{1}\bar{1}]$ is also 1NN to a_O but lies on the same plane as a_P and these cannot be paired up. Conversely, other vectors of different magnitude, such as $\frac{a_\gamma}{2}[1\bar{2}1]$, are 1NN to a_O and can be paired up with a_P to form a primitive basis. Following this, the vector selection algorithm is as follows:

(i) A_1 and B_1 are chosen as a 1NN vectors to A_0 and B_0, respectively, identifying the $A_0 - A_1$ and $B_0 - B_1$ planes forming, respectively.
(ii) A_i and B_j for $i, j > 1$ are chosen as 1NN on different planes to A_1 and B_1, respectively.
(iii) If there are not suitable 1NN candidates, A_i and B_j are chosen as 2NN or higher. Vectors outside the unit cell are only considered if there are no suitable candidates left.
(iv) Proceed to calculate s_i once all vectors are identified.

The equation for calculating second and higher nearest neighbours is:

$$d_{2NN} = \min(\|A_k - (A_k \cdot \hat{n}_{A_0})\hat{n}_{A_0}\|) \text{ for } d_{2NN} > d_{1NN} \text{ and } A_k \in \mathcal{A}$$
$$d_{pNN} = \min(\|A_l - (A_l \cdot \hat{n}_{A_0})\hat{n}_{A_0}\|) \text{ for } d_{pNN} > d_{(p-1)NN} \text{ and } A_l \in \mathcal{A} \quad (14)$$

A table with 1NN and 2NNs for typical directions in FCC, BCC and HCP crystals is presented in Appendix.

To illustrate how the vector selection process works, we return to the FCC→BCC crystal case. Tables 5 and 6 show the predicted calculations for $\boldsymbol{s}^{bain}$ and $\boldsymbol{s}^{lath}$ considering various 1NN and 2NN combinations when $B_0 = \frac{a_\alpha}{2}[111]$ (KS) and $B_0 = a_\alpha[100]$ (NW), respectively; also, $A_1 = a_P = \frac{a_\gamma}{2}[011]$, $B_1^{KS} = a_\alpha[001]$ and $B_1^{NW} = \frac{a_\alpha}{2}[111]$. We will concentrate on $\boldsymbol{s}^{bain}$ and $\boldsymbol{s}^{lath}$ for simplicity in the analysis but results for other extrema are equivalent. We assume $A_2 = a_Q$ and B_2^{KS} and B_2^{NW} as in Eq. (7) for computing T. Similar results were obtained for all 12 $\frac{1}{2}\langle 110\rangle_{FCC}$ systems (discussed below). Following the energy minimisation assumption, only the lowest strains are considered to be valid which are shown in bold in the table; other strains are not used as they do not represent minimum energy configurations, *e.g.* $\boldsymbol{s}^{bain} = 0.21$ nm for the pair 0.21 nm/0.38 nm in KS OR is greater or equal than $\boldsymbol{s}_{lath}$ for other vector configurations. For KS OR, 4 1NN vectors lie on the $(111)_{FCC}$ plane and, from a crystallographic stand point, choosing

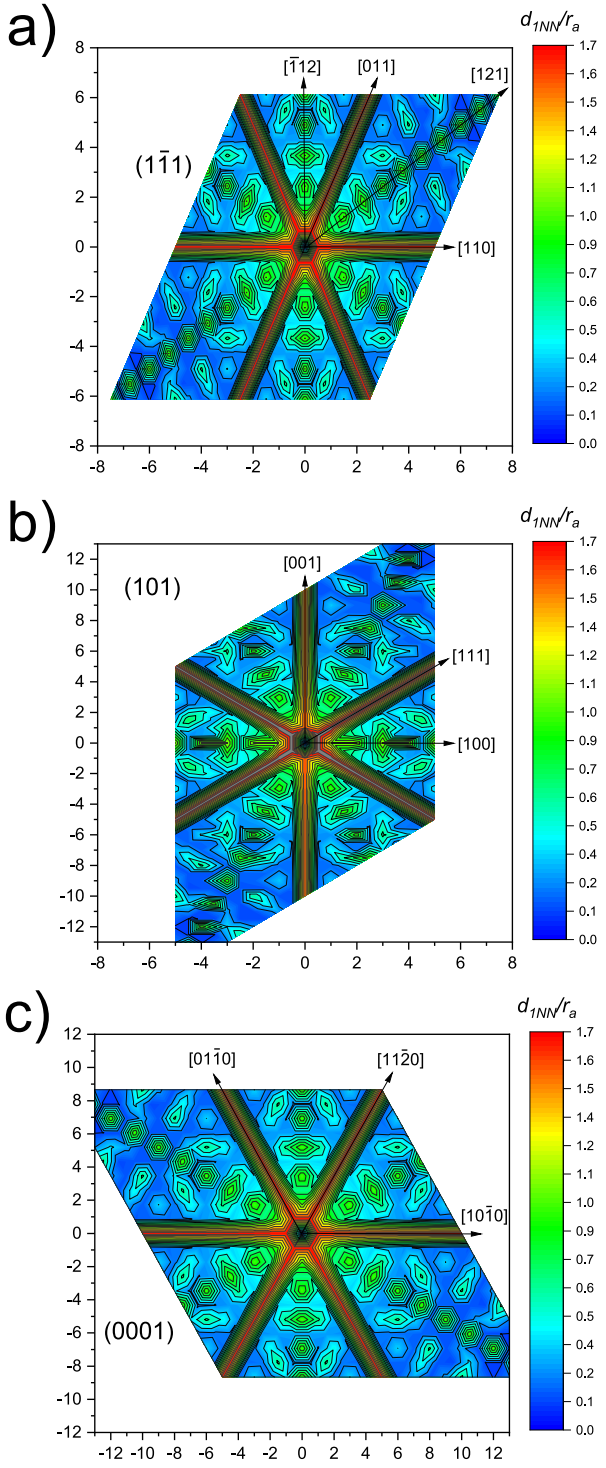

Fig. 5. Normalised 1st nearest neighbour distance calculations along closed packed planes for (a) FCC, (b) BCC and (c) HCP lattices in Fe.

any direction among these as variant would give equivalent results; however, the model predicts 2 different sets of strains indicating that 2 variants (directions) are involved in $[1\bar{1}0]_{FCC}\|[111]_{BCC}$. Interestingly, when comparing the results for NW OR, all 6 1NN directions lie on (111) and have the same strain values confirming that only 1 variant is present for $[1\bar{1}0]_{FCC}\|[100]_{BCC}$, *i.e.* the model successfully predicts KS and NW ORs have 24 and 12 variants, respectively, with each also having an associated strain and atomic path configuration. Moreover, when studying the results for the 2NN directions in FCC following KS OR, *i.e.* $[100]_{FCC}$ and $[010]_{FCC}$, the model predicts 2 low-energy set of strains for these directions lying on plane $(001)_{FCC}$; this plane combination matches Pitsch OR (Table 1). As for estimating the number of variants in Pitsch OR, s_1^P and s_2^P are identical in magnitude and direction to KS' and the only difference between these vectors is that s_2^P lies on $(001)_{FCC}$; since the planes forming between A_0 and A_1^P are already accounted for in KS OR, then the only planes/variants missing are those arising from $(001)_{FCC}$ planes forming by A_0 and A_2^P, which are 12 in total, one per each A_0 variant. Therefore, the model also successfully predicts Pitsch OR and its 12 variants, *i.e.* $\langle 1\bar{1}0\rangle_{FCC}\|\langle 111\rangle_{BCC}$ and $\{001\}_{FCC}\|\{110\}_{BCC}$, with their associated strains. The habit planes in Miller notation are computed following the same algorithm to obtain Eqs. (10) and (11) but now identifying the parallel directions of HP_i^j consistent with A_0 to obtain a similar ratio in each component (*e.g.* identifying that $HP_i^j \propto (l\ l\ k)$ for a_O as invariant direction gives the ratio $\frac{HP_{i,x}^j}{HP_{j,z}^j}$ in the z component).

As for configurations in the NW case, there is an additional set of minimum strain solutions when considering 2NN in the FCC phase. The associated directions for A_2^{FCC} are on the $(001)_{FCC}$ plane and for B_2 these lie on the family of $\{011\}_{BCC}$ planes. The predicted OR corresponds to a modified version of Bain's orientation relationship (Table 1) but only imposing 1 invariant direction. In this case the OR is: $\langle 1\bar{1}0\rangle_{FCC}\|\langle 100\rangle_{BCC}$ with $\{001\}_{FCC}\|\{0\bar{1}1\}_{BCC}$. The predicted shear directions for $A_2 = [0\bar{1}0]_{FCC}$ and $B_2 = [10\bar{1}]_{BCC}$ are $s_1 = [0.023, 0, -0.036]$ nm and $s_2 = [0, -0.02, -0.036]$ nm (although this vector selection is not considered as part of the OR due to being 2NN in the BCC phase, these directions are the closest match to Bain's original model); as illustrated by Fig. 3(a), these solutions represent almost symmetric and small dilatations along $[10\bar{1}]_{FCC}$ and $[0\bar{1}\bar{1}]_{FCC}$, respectively, in a similar fashion as Bain's strain derivation. To further corroborate the results, $\boldsymbol{s}^{bain}$ is compared against the standard strain calculations using Bain OR [1]. The Bain strain considering $[1\bar{1}0]_{FCC}$ as invariant line strain is obtained by calculating the necessary atomic displacements along $[1\bar{1}0]_{FCC}$, $[001]_{FCC}$, and $[100]_{FCC}$ to match the BCC unit cell, which respectively are [1]: $\eta_2 = a_\alpha - a_\gamma = -0.07$ nm, $\eta_1 = \eta_3 = a_\alpha - a_\gamma/\sqrt{2} = 0.0329$ nm; this gives a total displacement of $\sqrt{\eta_1^2+\eta_2^2+\eta_3^2} = 0.084$ nm, which is very close to $\boldsymbol{s}^{bain} = 0.068$ nm. Similar to the previous case, this Bain-like OR has 12 variants. This is because, although 2 different sets of shear values are predicted for $\boldsymbol{s}$, $\boldsymbol{s}_1^B$ are identical in each case and $\boldsymbol{s}_2^B$ are only slightly different, *e.g.* the same first shear vector $s_1^{bain} = [-0.025, -0.048, 0.009]$ nm is predicted when considering A_2 as $[0\bar{1}0]$ and [100], whereas the second vector is $s_2^{bain} = [-0.08, 0.09, 0.083]$ nm and $s_2^{bain} = [0.12, -0.10, 0.08]$ nm, respectively, indicating that there is only a small difference between them. In addition, both vector combinations lie on the same $(001)_{FCC}$ plane. Lastly, we note that the same solutions are obtained when including 2NN directions in the BCC phase ($\langle 311\rangle_{BCC}$) but these are not considered as they lie outside the unit cell and do not constitute primitive basis vectors.

Tables 7 and 8 show the predicted results for all variants in the KS/NW and Pitsch/Bain ORs, respectively. The tables show the vector bases used for each calculation, *i.e.* A_0, A_1 and A_2, the associated planes $P1_{FCC}/P2_{FCC}$ forming between A_0 and A_1/A_2, as well as the respective vectors and planes for the BCC product phase. Similar to previous cases, Eq. (5) are solved numerically changing one variable and finding the 4 extrema of the curved obtained. In addition, $\boldsymbol{s}^{bain}$ and $\boldsymbol{s}^{mart}$ are displayed to compare the strains induced per variant. For the case of KS and NW ORs, each vector set corresponds to primitive basis vectors, *i.e.* $A_i = a_i$, however for Pitsch and Bain ORs, the sets $\{A_i\}$ do not correspond to a primitive basis, particularly for $A_2^{P/B}$. In this case, the associated primitive vector a_2^j is taken same as A_2 in Table 7 to solve Eq. (5). Also, Table 8 shows average values for $\boldsymbol{s}^{bain}$ and $\boldsymbol{s}^{mart}$ as the 2 shear results are considered part of the same variant (Table 6). Two sets

Table 5
s^{lath} and s^{bain} obtained for different combinations of 1NN and 2NN for A_2 following KS OR: $A_0 = \frac{a_\gamma}{2}[1\bar{1}0]_{FCC}$ (rows) and $B_0 = \frac{a_\alpha}{2}[111]_{BCC}$ (columns), using $A_1 = \frac{a_\gamma}{2}[101]$ and $B_1 = a_\alpha[001]$, respectively.

		[0 1 0]	[1 0 0]	[0 1 1]	[1 0 1]	$\frac{1}{2}$[1 3 $\bar{1}$]	$\frac{1}{2}$[3 1 $\bar{1}$]	$\frac{1}{2}$[$\bar{1}$ 3 1]	$\frac{1}{2}$[3 $\bar{1}$ 1]	$\frac{1}{2}$[$\bar{1}$ 1 3]	$\frac{1}{2}$[1 $\bar{1}$ 3]
$\frac{1}{2}$[0 $\bar{1}$ 1]	s^{bain}	**0.148**	**0.148**	0.21	0.21	0.331	0.338	0.233	0.233	0.258	0.258
	s^{lath}	**0.217**	**0.217**	0.382	0.382	0.332	0.332	0.355	0.355	0.536	0.536
$\frac{1}{2}$[1 0 $\bar{1}$]	s^{bain}	**0.068**	**0.068**	0.253	0.253	0.261	0.261	0.236	0.236	0.334	0.334
	s^{lath}	**0.326**	**0.326**	0.298	0.298	0.537	0.537	0.357	0.357	0.334	0.334
$\frac{1}{2}$[1 $\bar{2}$ 1]	s^{bain}	0.253	0.253	**0.068**	**0.068**	0.333	0.333	0.236	0.235	0.261	0.2631
	s^{lath}	0.298	0.298	**0.326**	**0.326**	0.334	0.334	0.357	0.357	0.537	0.537
$\frac{1}{2}$[2 $\bar{1}$ $\bar{1}$]	s^{bain}	0.21	0.21	**0.148**	**0.148**	0.258	0.258	0.233	0.233	0.33	0.33
	s^{lath}	0.382	0.382	**0.217**	**0.217**	0.536	0.536	0.355	0.355	0.332	0.332
[0 $\bar{1}$ 0]	s^{bain}	**0.068**	**0.068**	0.258	0.258	**0.15**	**0.15**	0.256	0.256	0.437	0.437
	s^{lath}	**0.326**	**0.326**	0.536	0.536	**0.217**	**0.217**	0.476	0.476	0.742	0.742
[1 0 0]	s^{bain}	0.258	0.258	**0.068**	**0.068**	0.437	0.437	0.256	0.256	**0.15**	**0.15**
	s^{lath}	0.536	0.536	**0.326**	**0.3256**	0.742	0.742	0.476	0.476	**0.217**	**0.217**

Table 6
s^{lath} and s^{bain} for different combinations of 1NN and 2NN for A_2 following NW OR: $A_0 = \frac{a_\gamma}{2}[1\bar{1}0]_{FCC}$ (rows) and $B_0 = \frac{a_\alpha}{2}[100]_{BCC}$ (columns), using $A_1 = \frac{a_\gamma}{2}[101]_{FCC}$ and $B_1 = \frac{a_\alpha}{2}[111]_{BCC}$, respectively.

		$\frac{1}{2}$[1 1 $\bar{1}$]	$\frac{1}{2}$[1 $\bar{1}$ 1]	$\frac{1}{2}$[3 1 $\bar{1}$]	$\frac{1}{2}$[3 $\bar{1}$ 1]	[1 0 $\bar{1}$]	[1 $\bar{1}$ 0]	[1 1 0]	[1 0 1]
$\frac{1}{2}$[0 $\bar{1}$ 1]	s^{bain}	**0.06**	**0.06**	0.308	0.308	0.249	0.249	**0.188**	**0.188**
	s^{lath}	**0.234**	**0.234**	0.382	0.382	0.264	0.264	**0.414**	**0.414**
$\frac{1}{2}$[1 0 $\bar{1}$]	s^{bain}	**0.06**	**0.06**	0.275	0.275	**0.1619**	**0.1619**	0.23	0.23
	s^{lath}	**0.234**	**0.234**	0.356	0.356	**0.403**	**0.403**	0.245	0.245
$\frac{1}{2}$[1 $\bar{2}$ 1]	s^{bain}	0.275	0.275	**0.06**	**0.06**	0.23	0.23	**0.161**	**0.161**
	s^{lath}	0.356	0.356	**0.234**	**0.234**	0.245	0.245	**0.403**	**0.403**
$\frac{1}{2}$[2 $\bar{1}$ $\bar{1}$]	s^{bain}	0.308	0.308	**0.06**	**0.06**	**0.188**	**0.188**	0.249	0.249
	s^{lath}	0.382	0.382	**0.234**	**0.234**	**0.414**	**0.414**	0.264	0.264
[0 $\bar{1}$ 0]	s^{bain}	**0.161**	**0.161**	**0.188**	**0.188**	**0.06**	**0.06**	0.27	0.27
	s^{lath}	**0.403**	**0.403**	**0.414**	**0.414**	**0.234**	**0.234**	0.566	0.566
[1 0 0]	s^{bain}	**0.188**	**0.188**	**0.161**	**0.161**	0.27	0.27	**0.06**	**0.06**
	s^{lath}	**0.414**	**0.414**	**0.403**	**0.403**	0.566	0.566	**0.234**	**0.234**

Table 7
Variant selection and shear displacements for KS and NW ORs with $A_0||B_0^i$ and $P1_{FCC}||P1_{BCC}^i$ and $P2_{FCC}||P2_{BCC}^i$.

Variant	A_0	A_1	$A_2^{P/B}$	$P1_{FCC}$	$P2_{FCC}$	B_0^{KS}	B_1^{KS}	B_2^{KS}	$P1_{BCC}^{KS}$	$P2_{BCC}^{KS}$	$s^{bain,KS}/s^{mart,KS}$	B_0^{NW}	B_1^{NW}	B_2^{NW}	$P1_{BCC}^{NW}$	$P2_{BCC}^{NW}$	$s^{bain,NW}/s^{mart,NW}$
V1	$\frac{1}{2}$[1$\bar{1}$0]	$\frac{1}{2}$[101]	$\frac{1}{2}$[0$\bar{1}$1]	(11$\bar{1}$)	(111)	$\frac{1}{2}$[111]	[001]	[010]	(1$\bar{1}$0)	(01$\bar{1}$)	0.149/0.217	[100]	$\frac{1}{2}$[111]	$\frac{1}{2}$[11$\bar{1}$]	(0$\bar{1}$1)	(011)	0.06/0.23
V2	$\frac{1}{2}$[110]	$\frac{1}{2}$[011]	$\frac{1}{2}$[101]	($\bar{1}$11)	($\bar{1}$11)	$\frac{1}{2}$[111]	[001]	[010]	(1$\bar{1}$0)	(01$\bar{1}$)	0.149/0.217	[100]	$\frac{1}{2}$[111]	$\frac{1}{2}$[1$\bar{1}$1]	(0$\bar{1}$1)	(011)	0.06/0.23
V3	$\frac{1}{2}$[$\bar{1}$10]	$\frac{1}{2}$[$\bar{1}$01]	$\frac{1}{2}$[011]	(111)	(11$\bar{1}$)	$\frac{1}{2}$[111]	[001]	[010]	(1$\bar{1}$0)	(01$\bar{1}$)	0.149/0.217	[100]	$\frac{1}{2}$[111]	$\frac{1}{2}$[1$\bar{1}$1]	(0$\bar{1}$1)	(011)	0.06/0.23
V4	$\frac{1}{2}$[1$\bar{1}$0]	$\frac{1}{2}$[0$\bar{1}$1]	$\frac{1}{2}$[$\bar{1}$01]	($\bar{1}$11)	(1$\bar{1}$1)	$\frac{1}{2}$[111]	[001]	[010]	(1$\bar{1}$0)	(01$\bar{1}$)	0.149/0.217	[100]	$\frac{1}{2}$[111]	$\frac{1}{2}$[1$\bar{1}$1]	(0$\bar{1}$1)	(011)	0.06/0.23
V5	$\frac{1}{2}$[101]	$\frac{1}{2}$[1$\bar{1}$0]	$\frac{1}{2}$[110]	(11$\bar{1}$)	($\bar{1}$11)	$\frac{1}{2}$[111]	[001]	[010]	(1$\bar{1}$0)	(01$\bar{1}$)	0.0685/0.326	[100]	$\frac{1}{2}$[111]	$\frac{1}{2}$[1$\bar{1}$1]	(0$\bar{1}$1)	(011)	0.06/0.23
V6	$\frac{1}{2}$[011]	$\frac{1}{2}$[110]	$\frac{1}{2}$[$\bar{1}$10]	($\bar{1}$11)	(11$\bar{1}$)	$\frac{1}{2}$[111]	[001]	[010]	(1$\bar{1}$0)	(01$\bar{1}$)	0.0685/0.326	[100]	$\frac{1}{2}$[111]	$\frac{1}{2}$[1$\bar{1}$1]	(0$\bar{1}$1)	(011)	0.06/0.23
V7	$\frac{1}{2}$[$\bar{1}$01]	$\frac{1}{2}$[$\bar{1}$10]	$\frac{1}{2}$[1$\bar{1}$0]	(111)	($\bar{1}$11)	$\frac{1}{2}$[111]	[001]	[010]	(1$\bar{1}$0)	(01$\bar{1}$)	0.0685/0.326	[100]	$\frac{1}{2}$[111]	$\frac{1}{2}$[1$\bar{1}$1]	(0$\bar{1}$1)	(011)	0.06/0.23
V8	$\frac{1}{2}$[0$\bar{1}$1]	$\frac{1}{2}$[1$\bar{1}$0]	$\frac{1}{2}$[$\bar{1}$01]	($\bar{1}$11)	(111)	$\frac{1}{2}$[111]	[001]	[010]	(1$\bar{1}$0)	(01$\bar{1}$)	0.0685/0.326	[100]	$\frac{1}{2}$[111]	$\frac{1}{2}$[1$\bar{1}$1]	(0$\bar{1}$1)	(011)	0.06/0.23
V9	$\frac{1}{2}$[10$\bar{1}$]	$\frac{1}{2}$[110]	$\frac{1}{2}$[1$\bar{1}$0]	(1$\bar{1}$1)	(111)	$\frac{1}{2}$[111]	[001]	[010]	(1$\bar{1}$0)	(01$\bar{1}$)	0.0685/0.326	[100]	$\frac{1}{2}$[111]	$\frac{1}{2}$[1$\bar{1}$1]	(0$\bar{1}$1)	(011)	0.06/0.23
V10	$\frac{1}{2}$[01$\bar{1}$]	$\frac{1}{2}$[$\bar{1}$10]	$\frac{1}{2}$[110]	(111)	($\bar{1}$11)	$\frac{1}{2}$[111]	[001]	[010]	(1$\bar{1}$0)	(01$\bar{1}$)	0.0685/0.326	[100]	$\frac{1}{2}$[111]	$\frac{1}{2}$[1$\bar{1}$1]	(0$\bar{1}$1)	(011)	0.06/0.23
V11	$\frac{1}{2}$[0$\bar{1}$1]	$\frac{1}{2}$[1$\bar{1}$0]	$\frac{1}{2}$[$\bar{1}$10]	(11$\bar{1}$)	(1$\bar{1}$1)	$\frac{1}{2}$[111]	[001]	[010]	(1$\bar{1}$0)	(01$\bar{1}$)	0.0685/0.326	[100]	$\frac{1}{2}$[111]	$\frac{1}{2}$[1$\bar{1}$1]	(0$\bar{1}$1)	(011)	0.06/0.23
V12	$\frac{1}{2}$[$\bar{1}$0$\bar{1}$]	$\frac{1}{2}$[$\bar{1}$10]	$\frac{1}{2}$[$\bar{1}$10]	(1$\bar{1}$1)	(11$\bar{1}$)	$\frac{1}{2}$[111]	[001]	[010]	(1$\bar{1}$0)	(01$\bar{1}$)	0.0685/0.326	[100]	$\frac{1}{2}$[111]	$\frac{1}{2}$[1$\bar{1}$1]	(0$\bar{1}$1)	(011)	0.06/0.23
V13	$\frac{1}{2}$[1$\bar{1}$0]	$\frac{1}{2}$[101]	$\frac{1}{2}$[10$\bar{1}$]	(11$\bar{1}$)	(111)	$\frac{1}{2}$[111]	[001]	[010]	(1$\bar{1}$0)	(01$\bar{1}$)	0.0685/0.326						
V14	$\frac{1}{2}$[110]	$\frac{1}{2}$[011]	$\frac{1}{2}$[01$\bar{1}$]	(11$\bar{1}$)	($\bar{1}$11)	$\frac{1}{2}$[111]	[001]	[010]	(1$\bar{1}$0)	(01$\bar{1}$)	0.0685/0.326						
V15	$\frac{1}{2}$[$\bar{1}$10]	$\frac{1}{2}$[$\bar{1}$01]	$\frac{1}{2}$[$\bar{1}$0$\bar{1}$]	(111)	(11$\bar{1}$)	$\frac{1}{2}$[111]	[001]	[010]	(1$\bar{1}$0)	(01$\bar{1}$)	0.0685/0.326						
V16	$\frac{1}{2}$[1$\bar{1}$0]	$\frac{1}{2}$[0$\bar{1}$1]	$\frac{1}{2}$[0$\bar{1}$$\bar{1}$]	($\bar{1}$11)	(1$\bar{1}$1)	$\frac{1}{2}$[111]	[001]	[010]	(1$\bar{1}$0)	(01$\bar{1}$)	0.0685/0.326						
V17	$\frac{1}{2}$[101]	$\frac{1}{2}$[1$\bar{1}$0]	$\frac{1}{2}$[0$\bar{1}$1]	(11$\bar{1}$)	($\bar{1}$11)	$\frac{1}{2}$[111]	[001]	[010]	(1$\bar{1}$0)	(01$\bar{1}$)	0.149/0.217						
V18	$\frac{1}{2}$[011]	$\frac{1}{2}$[110]	$\frac{1}{2}$[101]	(1$\bar{1}$1)	(11$\bar{1}$)	$\frac{1}{2}$[111]	[001]	[010]	(1$\bar{1}$0)	(01$\bar{1}$)	0.149/0.217						
V19	$\frac{1}{2}$[$\bar{1}$01]	$\frac{1}{2}$[$\bar{1}$10]	$\frac{1}{2}$[011]	(111)	(1$\bar{1}$1)	$\frac{1}{2}$[111]	[001]	[010]	(1$\bar{1}$0)	(01$\bar{1}$)	0.149/0.217						
V20	$\frac{1}{2}$[0$\bar{1}$1]	$\frac{1}{2}$[$\bar{1}$10]	$\frac{1}{2}$[1$\bar{1}$0]	($\bar{1}$11)	(111)	$\frac{1}{2}$[111]	[001]	[010]	(1$\bar{1}$0)	(01$\bar{1}$)	0.149/0.217						
V21	$\frac{1}{2}$[10$\bar{1}$]	$\frac{1}{2}$[110]	$\frac{1}{2}$[01$\bar{1}$]	(1$\bar{1}$1)	(111)	$\frac{1}{2}$[111]	[001]	[010]	(1$\bar{1}$0)	(01$\bar{1}$)	0.149/0.217						
V22	$\frac{1}{2}$[01$\bar{1}$]	$\frac{1}{2}$[$\bar{1}$10]	$\frac{1}{2}$[$\bar{1}$01]	(111)	($\bar{1}$11)	$\frac{1}{2}$[111]	[001]	[010]	(1$\bar{1}$0)	(01$\bar{1}$)	0.149/0.217						
V23	$\frac{1}{2}$[0$\bar{1}$$\bar{1}$]	$\frac{1}{2}$[1$\bar{1}$0]	$\frac{1}{2}$[10$\bar{1}$]	(11$\bar{1}$)	(1$\bar{1}$1)	$\frac{1}{2}$[111]	[001]	[010]	(1$\bar{1}$0)	(01$\bar{1}$)	0.149/0.217						
V24	$\frac{1}{2}$[$\bar{1}$0$\bar{1}$]	$\frac{1}{2}$[$\bar{1}$10]	$\frac{1}{2}$[0$\bar{1}$$\bar{1}$]	(1$\bar{1}$1)	(11$\bar{1}$)	$\frac{1}{2}$[111]	[001]	[010]	(1$\bar{1}$0)	(01$\bar{1}$)	0.149/0.217						

of strains are predicted for KS OR with variants having the lowest shear values likely forming first, whereas one single set of strains are present in NW, Pitsch and Bain's OR, indicating no particular preference for what variant forms first.

Candidate invariant directions for GT OR ($\frac{1}{2}\langle 211\rangle_{FCC}$) are the only relations left to explore. Table 9 shows s^{lath} and s^{bain} values computed using $A_0^{GT} = \frac{a_\gamma}{2}[2\bar{1}1]$, $A_1^{GT} = a_P$, $B_0^{GT} = a_\alpha[110]$ and $B_1^{GT} = \frac{a_\alpha}{2}[111]$. Only 2NN directions are predicted for A_2^{GT} and B_2^{GT} and all solutions for A_2^{GT} and B_2^{GT} lie on (011) and (001) planes, respectively, indicating the following orientation relationships $\langle 211\rangle_{FCC}\|\langle 110\rangle_{BCC}$, $\{111\}_{FCC}\|\{110\}_{BCC}$ and $\{011\}_{FCC}\|\{001\}_{BCC}$. Similar to KS OR, two sets of strains are computed indicating that 2 variants are present for this choice of invariant directions. Therefore, since $\langle 211\rangle_{FCC}$ has 12 systems, all 24 variants of the GT OR are successfully predicted.

Table 8
Variant selection and shear displacements for Pitsch and Bain ORs with $A_0 || B_0^i$ and $P1_{FCC} || P1^i_{BCC}$ and $P2_{FCC} || P2^i_{BCC}$.

Variant	A_0	A_1	A_2	$P1_{FCC}$	$P2_{FCC}$	B_0^P	B_1^P	B_2^P	$P1^P_{BCC}$	$P2^P_{BCC}$	$s^{bain,P}/s^{mart,P}$	B_0^B	B_1^B	B_2^B	$P1^B_{BCC}$	$P2^B_{BCC}$	$s^{bain,B}/s^{mart,B}$
V1	$\frac{1}{2}[1\bar{1}0]$	$\frac{1}{2}[101]$	$[0\bar{1}0]$	$(11\bar{1})$	(001)	$\frac{1}{2}[111]$	[001]	[010]	$(1\bar{1}0)$	$(10\bar{1})$	0.0685/0.326	[100]	$\frac{1}{2}[111]$	$\frac{1}{2}[11\bar{1}]$	$(0\bar{1}1)$	(011)	0.17/0.409*
V2	$\frac{1}{2}[110]$	$\frac{1}{2}[011]$	[100]	$(1\bar{1}1)$	(001)	$\frac{1}{2}[111]$	[001]	[010]	$(1\bar{1}0)$	$(10\bar{1})$	0.0685/0.326	[100]	$\frac{1}{2}[111]$	$\frac{1}{2}[11\bar{1}]$	$(0\bar{1}1)$	(011)	0.17/0.409*
V3	$\frac{1}{2}[\bar{1}10]$	$\frac{1}{2}[\bar{1}01]$	[010]	(111)	(001)	$\frac{1}{2}[111]$	[001]	[010]	$(1\bar{1}0)$	$(10\bar{1})$	0.0685/0.326	[100]	$\frac{1}{2}[111]$	$\frac{1}{2}[11\bar{1}]$	$(0\bar{1}1)$	(011)	0.17/0.409*
V4	$\frac{1}{2}[\bar{1}\bar{1}0]$	$\frac{1}{2}[0\bar{1}1]$	$[\bar{1}00]$	$(\bar{1}11)$	(001)	$\frac{1}{2}[111]$	[001]	[010]	$(1\bar{1}0)$	$(10\bar{1})$	0.0685/0.326	[100]	$\frac{1}{2}[111]$	$\frac{1}{2}[11\bar{1}]$	$(0\bar{1}1)$	(011)	0.17/0.409*
V5	$\frac{1}{2}[101]$	$\frac{1}{2}[1\bar{1}0]$	[001]	$(11\bar{1})$	(010)	$\frac{1}{2}[111]$	[001]	[010]	$(1\bar{1}0)$	$(10\bar{1})$	0.0685/0.326	[100]	$\frac{1}{2}[111]$	$\frac{1}{2}[11\bar{1}]$	$(0\bar{1}1)$	(011)	0.17/0.409*
V6	$\frac{1}{2}[011]$	$\frac{1}{2}[110]$	[001]	$(1\bar{1}1)$	(100)	$\frac{1}{2}[111]$	[001]	[010]	$(1\bar{1}0)$	$(10\bar{1})$	0.0685/0.326	[100]	$\frac{1}{2}[111]$	$\frac{1}{2}[11\bar{1}]$	$(0\bar{1}1)$	(011)	0.17/0.409*
V7	$\frac{1}{2}[\bar{1}01]$	$\frac{1}{2}[\bar{1}10]$	[001]	(111)	(010)	$\frac{1}{2}[111]$	[001]	[010]	$(1\bar{1}0)$	$(10\bar{1})$	0.0685/0.326	[100]	$\frac{1}{2}[111]$	$\frac{1}{2}[11\bar{1}]$	$(0\bar{1}1)$	(011)	0.17/0.409*
V8	$\frac{1}{2}[0\bar{1}1]$	$\frac{1}{2}[\bar{1}\bar{1}0]$	[001]	$(\bar{1}11)$	(100)	$\frac{1}{2}[111]$	[001]	[010]	$(1\bar{1}0)$	$(10\bar{1})$	0.0685/0.326	[100]	$\frac{1}{2}[111]$	$\frac{1}{2}[11\bar{1}]$	$(0\bar{1}1)$	(011)	0.17/0.409*
V9	$\frac{1}{2}[10\bar{1}]$	$\frac{1}{2}[110]$	$[00\bar{1}]$	$(1\bar{1}1)$	(010)	$\frac{1}{2}[111]$	[001]	[010]	$(1\bar{1}0)$	$(10\bar{1})$	0.0685/0.326	[100]	$\frac{1}{2}[111]$	$\frac{1}{2}[11\bar{1}]$	$(0\bar{1}1)$	(011)	0.17/0.409*
V10	$\frac{1}{2}[01\bar{1}]$	$\frac{1}{2}[\bar{1}10]$	$[00\bar{1}]$	(111)	(100)	$\frac{1}{2}[111]$	[001]	[010]	$(1\bar{1}0)$	$(10\bar{1})$	0.0685/0.326	[100]	$\frac{1}{2}[111]$	$\frac{1}{2}[11\bar{1}]$	$(0\bar{1}1)$	(011)	0.17/0.409*
V11	$\frac{1}{2}[0\bar{1}1]$	$\frac{1}{2}[1\bar{1}0]$	$[00\bar{1}]$	$(11\bar{1})$	(100)	$\frac{1}{2}[111]$	[001]	[010]	$(1\bar{1}0)$	$(10\bar{1})$	0.0685/0.326	[100]	$\frac{1}{2}[111]$	$\frac{1}{2}[11\bar{1}]$	$(0\bar{1}1)$	(011)	0.17/0.409*
V12	$\frac{1}{2}[\bar{1}0\bar{1}]$	$\frac{1}{2}[\bar{1}\bar{1}0]$	$[00\bar{1}]$	$(1\bar{1}1)$	(010)	$\frac{1}{2}[111]$	[001]	[010]	$(1\bar{1}0)$	$(10\bar{1})$	0.0685/0.326	[100]	$\frac{1}{2}[111]$	$\frac{1}{2}[11\bar{1}]$	$(0\bar{1}1)$	(011)	0.17/0.409*

Table 9
s^{lath} and s^{bain} for different combinations of 1NN and 2NN for A_2 and B_2 following GT OR.

		[1 0 0]	[0 1 0]	[2 1 0]	[1 2 0]
[1 0 0]	s_{bain}	**0.047**	**0.047**	0.366	0.366
	s_{lath}	**0.407**	**0.407**	0.546	0.546
[1 $\bar{1}$ 1]	s_{bain}	0.332	0.332	**0.077**	**0.077**
	s_{lath}	0.508	0.508	**0.392**	**0.392**

In addition, Fig. 6(a) shows the total shear plots for the 2 variants. Eq. (5) are solved with respect to x_1 using 1NN vectors displayed in Table 9 (Variants 1/13). The figure shows that solutions for the 2 variants are very similar and symmetric with respect to x_1. It also shows that $s^{lath,GT} \simeq s^{plate,GT} = 0.40$ nm; although $s^{lath,GT} > a_\gamma$, twinning does not operate as $s_i^{lath,GT} < a_\gamma$. The corresponding shear directions and habit planes predicted for the first variant ($s^{bain,GT} = 0.047$ nm) are: $s_1^{bain,GT} = [-0.015, 0.0174, 0.0058]$ nm, $s_2^{bain,GT} = [0.0334, -0.0048, 0.0242]$ nm, $s_1^{lath,GT} = [0.068, 0, -0.179]$ nm, $s_2^{lath,GT} = [0.23, 0.23, -0.13]$ nm and $HP_1^{bain,GT} = (-0.57, -0.65, 0.49)$ (or $(\overline{1.1}\ \ \bar{1}\ \ 1.3)$ in Miller indices), $HP_2^{bain,GT} = (-0.56, -0.43, 0.69)$ (or $(\overline{1.2}\ \ \overline{1.6}\ \ 1)$), $HP_1^{lath,GT} = (0.38, 0.91, 0.14)$ (or (4.78 2 13)) and $HP_2^{lath,GT} = (-0.12, 0.57, 0.81)$ (or $(\overline{13}\ \ 2.8\ \ 2)$) . For the second variant ($s^{bain,GT} = 0.077$ nm), the following were obtained: $s_1^{bain,GT} = [-0.008, 0.02, -0.001]$ nm, $s_2^{bain,GT} = [0.05, -0.034, 0.031]$ nm, $s_1^{lath,GT} = [0.068, 0, -0.179]$ nm, $s_2^{lath,GT} = [0.09, 0.23, 0.22]$ nm and $HP_1^{bain,GT} = (-0.48, -0.1, 0.86)$ (or $(\overline{3.5}\ \ \overline{17.2}\ \ 2)$), $HP_2^{bain,GT} = (-0.16, -0.51, -0.84)$ (or $(\overline{10.5}\ \ \overline{3.2}\ \ \bar{2})$), $HP_1^{lath,GT} = (0.38, 0.91, 0.14)$ ((or (4.78 2 13)) and $HP_2^{lath,GT} = (-0.56, -0.43, 0.7)$ (or $\overline{6.2}\ \overline{8.1}\ 5$). The habit planes for $s^{lath,GT}$ are very close to the remaining habit planes previously reported in martensite (2 5 9) (or (0.9,0.36,0.2) in cartesian coordinates) and (3 10 15) (or (0.94,0.28,0.18)), respectively [2], whereas those for $s^{bain,GT}$ are $\sim 6°$ from {111}, also in agreement with experiments [1]. In addition, Table 10 shows the vector combinations to calculate all 24 variants in GT OR. Similar to the previous ORs, the table shows the vectors used in T, as well as their associated primitive bases (A_1^{GT} and A_2^{GT} are not primitive vectors), forming planes and shear magnitudes. Interestingly, in this case 6 sets of shear values are predicted, compared to the previous ORs. This can be associated to the fact that A_0^{GT} and A_2^{GT} are not primitive vectors and that there are different basis vector combinations that give similar strain values. It is also worth noting that the strain values in each variant can be obtained in others by using different vector basis combinations (a_i^{GT}). In summary, and to the author's knowledge, this is the first time that all reported ORs in FCC→BCC and habit planes for martensite and other shear transformations in Fe are simultaneously explained and predicted.

4.2. Orientation maps: connecting ORs and determining macroscopic structures

Orientation relationships represent misorientations between orientations of the parent and product phases and it is possible to study the spread in misorientations resulting from the predictions. Figs. 7(a) and 8(b) show $(100)_{BCC}$ pole figures including all predicted shears and their associated variants for s^{bain} and s^{lath}, respectively. Two points per variant are shown to represent the misorientations induced by s_1 and s_2. The procedure for calculating each misorientation point is as follows: first obtain $\tilde{B}_i^j$ for the respective variant and find the closet vector $\tilde{A}_j^j$ in the FCC lattice to obtain the angle θ_i^j and direction $p_i^j = (\tilde{B}_i^j - \tilde{A}_j^j)/\|\tilde{B}_i^j - \tilde{A}_j^j\|$ between the original and final vector positions inducing the respective misorientation. These values are then used to define the respective rotation matrix $R_{\theta_i^j}$ and compute $R_{\theta_i^j}[001]_{BCC}$, which is plotted in the Figures. Ideal ORs are also shown for comparison [10,62] and circles at $r = 0.1$ are included is as a guide to the eye. The misorientation distribution is similar between structures, but misorientations for s^{lath} are somewhat more pronounced, which is consistent with $s^{lath} > s^{bain}$, as the degree of misorientation is proportional to the shear magnitude. In addition, several variants are close to their theoretical counterparts with Pitsch and KS – as well as NW and Bain ORs – being close to each other due to their variants sharing the same s_1 values. Interestingly, the figures also show that there are direct paths connecting all ORs, *e.g* V10; this has been verified experimentally where the distribution in KS, NW, P and GT ORs exhibit continuous gradients with very similar proportion among each OR [7,79]. In addition, Figs. 7 and 8(b)-(f) respectively show individual variant distributions for KS, NW, Pitsch, Bain and GT ORs. For this particular choice of parameters, several variants tend to spread along $[1,1,0]_{BCC}$ and $[1,-1,0]_{BCC}$. These corresponds to KS/Pitsch variants of the form $\langle 011\rangle_{FCC}$ and $\langle 110\rangle_{FCC}$ for NW/Bain's. As for GT, variants are of the form $\langle 121\rangle$ and $\langle 112\rangle$. These results confirm the empirical argument that several ORs form within a single variant during the transformation. As indicated by Thome et al. [11], the orientation of each martensite variant is not only affected by the tendency to establish one specific OR but in fact there are several forming locally and the detection of a specific OR will depend on the location of the sampling region. This also implies that there is not a particular preference for one OR forming over another, at least for low alloyed metals, which is consistent with experimental findings for steels with different carbon content [79].

The fact that – macroscopically – there is no preference for ORs forming during the phase transformation process means that the microstructures forming are a result of the "average" processes occurring in each OR. In the previous sections it was demonstrated that the theory is able to predict all local crystallographic features of Widmanstätten ferrite and Bainite for s^{bain} but it was not possible to differentiate why and when these appear. Widmanstätten Ferrite mostly appears as

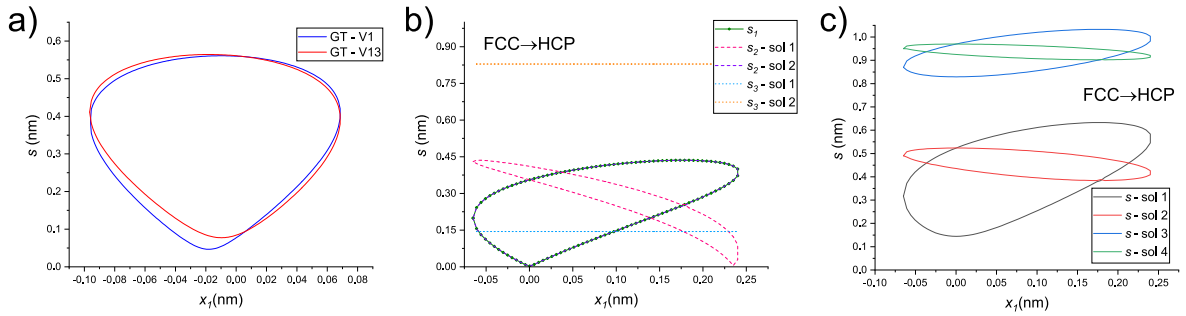

Fig. 6. (a) Total displacements *s* for 2 variants following GT OR. (b) Individual and (c) total shear displacements for the FCC→HCP transition in Fe.

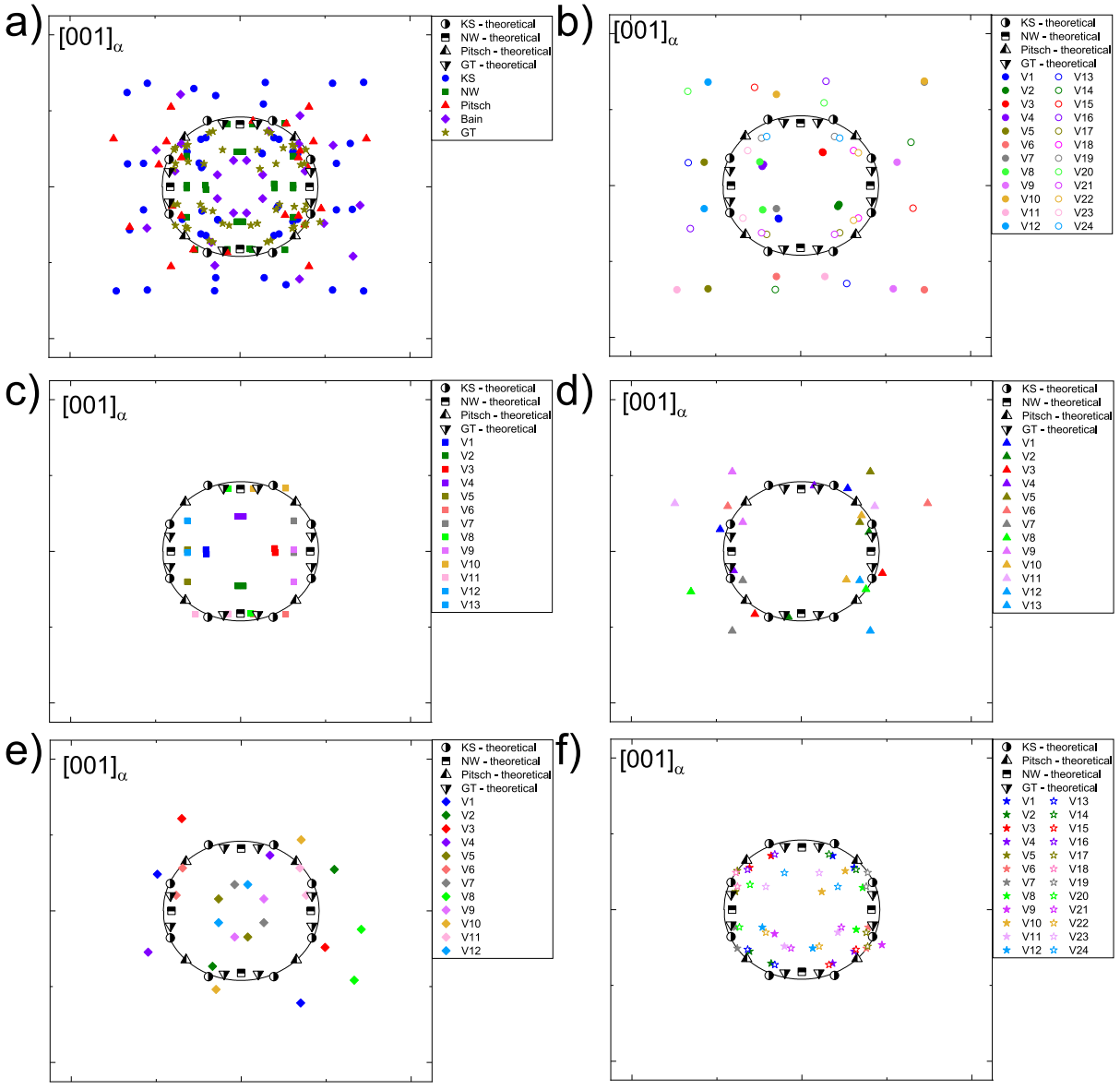

Fig. 7. (a) Pole figure showing ORs as misorientations about $[001]_{BCC}$ for s^{bain}. Variant distribution for (b) KS, (c) NW, (d) Pitsch, (e) Bain-like and (f) GT ORs.

Table 10
Variant selection and shear displacements for GT OR.

Variant	A_0^{GT}	A_1^{GT}	A_2^{GT}	a_0	a_1	a_2	$P1_{FCC}$	$P2_{FCC}$	B_0^{GT}	B_1^{GT}	B_2^{GT}	$P1_{BCC}^{GT}$	$P2_{BCC}^{GT}$	$s^{bain,GT}/s^{mart,GT}$
V1	$\frac{1}{2}[2\bar{1}1]$	$\frac{1}{2}[101]$	[100]	$\frac{1}{2}[1\bar{1}0]$	$\frac{1}{2}[101]$	$\frac{1}{2}[0\bar{1}1]$	$(11\bar{1})$	(011)	[110]	$\frac{1}{2}[111]$	[100]	$(1\bar{1}0)$	(001)	0.047/0.407
V2	$\frac{1}{2}[\bar{2}11]$	$\frac{1}{2}[\bar{1}01]$	$[\bar{1}00]$	$\frac{1}{2}[\bar{1}10]$	$\frac{1}{2}[\bar{1}01]$	$\frac{1}{2}[011]$	(111)	$(01\bar{1})$	[110]	$\frac{1}{2}[111]$	[100]	$(1\bar{1}0)$	(001)	0.047/0.407
V3	$\frac{1}{2}[21\bar{1}]$	$\frac{1}{2}[10\bar{1}]$	[100]	$\frac{1}{2}[110]$	$\frac{1}{2}[10\bar{1}]$	$\frac{1}{2}[01\bar{1}]$	$(1\bar{1}1)$	(011)	[110]	$\frac{1}{2}[111]$	[100]	$(1\bar{1}0)$	(001)	0.047/0.407
V4	$\frac{1}{2}[\bar{2}11]$	$\frac{1}{2}[1\bar{1}0]$	$[\bar{1}00]$	$\frac{1}{2}[1\bar{1}0]$	$\frac{1}{2}[\bar{1}0\bar{1}]$	$\frac{1}{2}[0\bar{1}\bar{1}]$	$(\bar{1}11)$	$(01\bar{1})$	[110]	$\frac{1}{2}[111]$	[100]	$(1\bar{1}0)$	(001)	0.047/0.407
V5	$\frac{1}{2}[121]$	$\frac{1}{2}[011]$	[010]	$\frac{1}{2}[110]$	$\frac{1}{2}[011]$	$\frac{1}{2}[101]$	$(1\bar{1}1)$	$(\bar{1}01)$	[110]	$\frac{1}{2}[111]$	[100]	$(1\bar{1}0)$	(001)	0.134/0.32
V6	$\frac{1}{2}[\bar{1}21]$	$\frac{1}{2}[0\bar{1}1]$	$[0\bar{1}0]$	$\frac{1}{2}[\bar{1}10]$	$\frac{1}{2}[0\bar{1}1]$	$\frac{1}{2}[\bar{1}01]$	$(\bar{1}11)$	(101)	[110]	$\frac{1}{2}[111]$	[100]	$(1\bar{1}0)$	(001)	0.134/0.32
V7	$\frac{1}{2}[\bar{1}21]$	$\frac{1}{2}[01\bar{1}]$	[010]	$\frac{1}{2}[\bar{1}10]$	$\frac{1}{2}[01\bar{1}]$	$\frac{1}{2}[\bar{1}0\bar{1}]$	(111)	$(\bar{1}01)$	[110]	$\frac{1}{2}[111]$	[100]	$(1\bar{1}0)$	(001)	0.134/0.32
V8	$\frac{1}{2}[1\bar{2}1]$	$\frac{1}{2}[1\bar{1}0]$	$[0\bar{1}0]$	$\frac{1}{2}[0\bar{1}\bar{1}]$	$\frac{1}{2}[1\bar{1}0]$	$\frac{1}{2}[10\bar{1}]$	$(11\bar{1})$	(101)	[110]	$\frac{1}{2}[111]$	[100]	$(1\bar{1}0)$	(001)	0.134/0.32
V9	$\frac{1}{2}[1\bar{1}2]$	$\frac{1}{2}[0\bar{1}1]$	[001]	$\frac{1}{2}[1\bar{1}0]$	$\frac{1}{2}[0\bar{1}1]$	$\frac{1}{2}[101]$	$(\bar{1}11)$	(110)	[110]	$\frac{1}{2}[111]$	[100]	$(1\bar{1}0)$	(001)	0.167/0.43
V10	$\frac{1}{2}[112]$	$\frac{1}{2}[011]$	[001]	$\frac{1}{2}[110]$	$\frac{1}{2}[011]$	$\frac{1}{2}[101]$	$(11\bar{1})$	$(1\bar{1}0)$	[110]	$\frac{1}{2}[111]$	[100]	$(1\bar{1}0)$	(001)	0.167/0.43
V11	$\frac{1}{2}[\bar{1}12]$	$\frac{1}{2}[011]$	[001]	$\frac{1}{2}[\bar{1}10]$	$\frac{1}{2}[011]$	$\frac{1}{2}[\bar{1}01]$	$(1\bar{1}1)$	(110)	[110]	$\frac{1}{2}[111]$	[100]	$(1\bar{1}0)$	(001)	0.167/0.43
V12	$\frac{1}{2}[\bar{1}\bar{1}2]$	$\frac{1}{2}[0\bar{1}1]$	[001]	$\frac{1}{2}[\bar{1}\bar{1}0]$	$\frac{1}{2}[0\bar{1}1]$	$\frac{1}{2}[\bar{1}01]$	(111)	$(1\bar{1}0)$	[110]	$\frac{1}{2}[111]$	[100]	$(1\bar{1}0)$	(001)	0.167/0.43
V13	$\frac{1}{2}[\bar{2}11]$	$\frac{1}{2}[\bar{1}0\bar{1}]$	$[\bar{1}00]$	$\frac{1}{2}[\bar{1}10]$	$\frac{1}{2}[\bar{1}0\bar{1}]$	$\frac{1}{2}[10\bar{1}]$	$(11\bar{1})$	(011)	[110]	$\frac{1}{2}[111]$	[100]	$(1\bar{1}0)$	(001)	0.077/0.392
V14	$\frac{1}{2}[2\bar{1}\bar{1}]$	$\frac{1}{2}[10\bar{1}]$	[100]	$\frac{1}{2}[1\bar{1}0]$	$\frac{1}{2}[10\bar{1}]$	$\frac{1}{2}[\bar{1}0\bar{1}]$	(111)	$(01\bar{1})$	[110]	$\frac{1}{2}[111]$	[100]	$(1\bar{1}0)$	(001)	0.077/0.392
V15	$\frac{1}{2}[\bar{2}11]$	$\frac{1}{2}[\bar{1}01]$	$[\bar{1}00]$	$\frac{1}{2}[\bar{1}\bar{1}0]$	$\frac{1}{2}[\bar{1}01]$	$\frac{1}{2}[101]$	$(1\bar{1}1)$	(011)	[110]	$\frac{1}{2}[111]$	[100]	$(1\bar{1}0)$	(001)	0.077/0.392
V16	$\frac{1}{2}[211]$	$\frac{1}{2}[110]$	[100]	$\frac{1}{2}[110]$	$\frac{1}{2}[101]$	$\frac{1}{2}[\bar{1}01]$	$(\bar{1}11)$	$(01\bar{1})$	[110]	$\frac{1}{2}[111]$	[100]	$(1\bar{1}0)$	(001)	0.077/0.392
V17	$\frac{1}{2}[\bar{1}21]$	$\frac{1}{2}[0\bar{1}1]$	$[0\bar{1}0]$	$\frac{1}{2}[\bar{1}10]$	$\frac{1}{2}[0\bar{1}1]$	$\frac{1}{2}[01\bar{1}]$	(111)	$(\bar{1}01)$	[110]	$\frac{1}{2}[111]$	[100]	$(1\bar{1}0)$	(001)	0.148/0.428
V18	$\frac{1}{2}[12\bar{1}]$	$\frac{1}{2}[01\bar{1}]$	[010]	$\frac{1}{2}[110]$	$\frac{1}{2}[01\bar{1}]$	$\frac{1}{2}[0\bar{1}1]$	$(11\bar{1})$	(101)	[110]	$\frac{1}{2}[111]$	[100]	$(1\bar{1}0)$	(001)	0.148/0.428
V19	$\frac{1}{2}[1\bar{2}1]$	$\frac{1}{2}[0\bar{1}1]$	$[0\bar{1}0]$	$\frac{1}{2}[1\bar{1}0]$	$\frac{1}{2}[0\bar{1}1]$	$\frac{1}{2}[011]$	$(1\bar{1}1)$	$(10\bar{1})$	[110]	$\frac{1}{2}[111]$	[100]	$(1\bar{1}0)$	(001)	0.148/0.428
V20	$\frac{1}{2}[\bar{1}21]$	$\frac{1}{2}[\bar{1}10]$	[010]	$\frac{1}{2}[011]$	$\frac{1}{2}[\bar{1}10]$	$\frac{1}{2}[\bar{1}\bar{1}0]$	$(\bar{1}11)$	(101)	[110]	$\frac{1}{2}[111]$	[100]	$(1\bar{1}0)$	(001)	0.148/0.428
V21	$\frac{1}{2}[\bar{1}\bar{1}2]$	$\frac{1}{2}[01\bar{1}]$	$[00\bar{1}]$	$\frac{1}{2}[\bar{1}10]$	$\frac{1}{2}[01\bar{1}]$	$\frac{1}{2}[0\bar{1}\bar{1}]$	$(\bar{1}11)$	(110)	[110]	$\frac{1}{2}[111]$	[100]	$(1\bar{1}0)$	(001)	0.148/0.428
V22	$\frac{1}{2}[\bar{1}\bar{1}2]$	$\frac{1}{2}[0\bar{1}\bar{1}]$	$[00\bar{1}]$	$\frac{1}{2}[\bar{1}\bar{1}0]$	$\frac{1}{2}[0\bar{1}\bar{1}]$	$\frac{1}{2}[01\bar{1}]$	$(11\bar{1})$	$(1\bar{1}0)$	[110]	$\frac{1}{2}[111]$	[100]	$(1\bar{1}0)$	(001)	0.148/0.428
V23	$\frac{1}{2}[1\bar{1}2]$	$\frac{1}{2}[0\bar{1}\bar{1}]$	$[00\bar{1}]$	$\frac{1}{2}[1\bar{1}0]$	$\frac{1}{2}[0\bar{1}\bar{1}]$	$\frac{1}{2}[01\bar{1}]$	$(1\bar{1}1)$	(110)	[110]	$\frac{1}{2}[111]$	[100]	$(1\bar{1}0)$	(001)	0.148/0.428
V24	$\frac{1}{2}[11\bar{2}]$	$\frac{1}{2}[01\bar{1}]$	$[00\bar{1}]$	$\frac{1}{2}[110]$	$\frac{1}{2}[01\bar{1}]$	$\frac{1}{2}[0\bar{1}\bar{1}]$	(111)	$(\bar{1}10)$	[110]	$\frac{1}{2}[111]$	[100]	$(1\bar{1}0)$	(001)	0.148/0.428

discrete plates, normally within a ferritic or pearlitic matrix, whereas Bainite normally forms as a large collection of laths/plates covering grain interiors — although it may also form various shapes depending on chemical composition. In addition, since we have shown that each complementary variant has different shear displacement values, *e.g.* $s^{bain,KS} = 0.148$ nm and 0.068 nm for V1 and V13 respectively, macroscopically the net displacement – or shear strain – should manifest as the average shear values, *i.e.* the macroscopic crystallographic features and shear values should correspond to the average values computed for all ORs. However, computing their average is not direct as not all vector combinations of different ORs are compatible. To this end, s_1^i (associated to A_1) is the only shear component that can be averaged as it has the same vector values in all ORs; s_2^i and A_2 involve using different vector combinations and resulting OR planes. Additionally, we leave the results GT OR out of the calculations as the vector selection is different for this OR. Table 11 shows the average for s_1^i with ORs having different vector values (duplicate vector values of different OR are not included). In addition, the table shows the habit plane of the resulting average direction for $\bar{s}_1^{bain} = \sum_i s_1^{bain,i}/5$ in Cartesian coordinates and Miller indices (note that the habit plane of the average shear is not the same than the average of individual habit planes), as well as the average shear values $\bar{s}^{bain} = \sum_i s^{bain,i}/5$. The habit plane of the average shear is equal to the habit plane of Bainite, *i.e.* (223) (in Miller indices) or (0.64,0.64,0.42), demonstrating that indeed the model predicts that Bainite corresponds to the macroscopic minimum energy configuration also forming as a bulk phase with macroscopic shear displacement 0.125 nm, whereas Widmanstätten Ferrite corresponds to the local minimum energy configuration, *e.g.* V13 in KS/P, with microscopic displacement as ∼ 0.06 nm (Average of KS and NW cases). To further corroborate the results, average values for s_1^{lath} and s^{lath}, *i.e.* lath martensite, are also computed and displayed in Table 11. The habit plane of the average shear is equal to the macroscopic habit plane of lath martensite, *i.e.* (557) (in Miller indices) or (0.63,0.63,0.45) . Further evidence supporting this conclusion is presented in Section 5 when computing the Thermodynamics of these transitions. In summary, this section has demonstrated that the theory is able to predict the local and macroscopic crystallographic features and atomic paths of Widmanstätten Ferrite, Bainite and Lath martensite and a similar argument could be made for plate and lenticular martensite. Such features have been described as consequence of predicting the arising ORs of the FCC→BCC phase transformations, which also show direct paths connecting individual variants in each OR. We now proceed generalise the theory when Crystal Lattices have different dimensions and apply it to FCC→HCP transformation in Fe.

4.3. Crystal lattices of different dimensions: Application to the FCC→HCP phase transformation

We now assume that $dim(\mathcal{A}) = N_A$ and $dim(\mathcal{B}) = N_B$ with $N_A \neq N_B$. Let us first study the case $N_A < N_B$, *e.g.* FCC/BCC→HCP. There are N_A basis vectors $\{a_i\}$ in $\mathcal{A}$ where the transformation can be defined as before in terms of the basis vectors: $T(a_0) = R(a_0 + \delta\hat{n}_0) = b_0$ and $T(a_i) = R(a_i + s_i) = b_i$ for $i = 1, \dots, N_A - 1$. For the remaining basis vectors in $\mathcal{B}$, *i.e.* b_j with $j = N_A ... N_B - 1$, there must exist a non-basis vector $a_j \in \mathcal{A}$ such that $T(a_j) = b_j$ to guarantee the transformation function is injective. a_j can be written as $a_j = \sum_{i=0}^{N_A-1} N_{i,j} a_i$ and, since $\sum_{i=0,i\neq j}^{N_A-1} N_{i,j} T(a_i) = \sum_{i=0,i\neq j}^{N_A-1} N_{i,j} b_i$ cannot generate b_j, we need to include an additional shear function s_j for $T(a_j)$, *i.e.* :

$$T(a_j) = b_j = R\left(\sum_i N_{i,j} T(a_i) + s_j\right) = R\left(a_j + \sum_i N_{i,j} s_i + s_j\right) \text{ with}$$
$$a_j = \sum_i N_{i,j} a_i, \; j = N_A ..., N_B - 1 \tag{15}$$

where $s_k \neq s_j$. We now have $3N_B+1$ equations for N_B-1 shear vectors, s_i and s_j, and δ, which can be solved using the same geometric relations for the vector dimensions and orientations in $\mathcal{B}$ and the extremum principle, as in Eqs. (5) and (6).

For the case $N_A > N_B$, *i.e.* when there are more basis vectors in the parent than the product phase such as HCP→FCC/BCC, we know that $T(a_j) = b_j = \sum_i N_{i,j} b_i = \sum_i N_{i,j} R(a_i + s_i)$ with $j > i$. On the other hand, the definition of the transformation function T gives $T(a_j) = R(a_j + s_j)$. Comparing the previous equations, the remaining shear vectors are

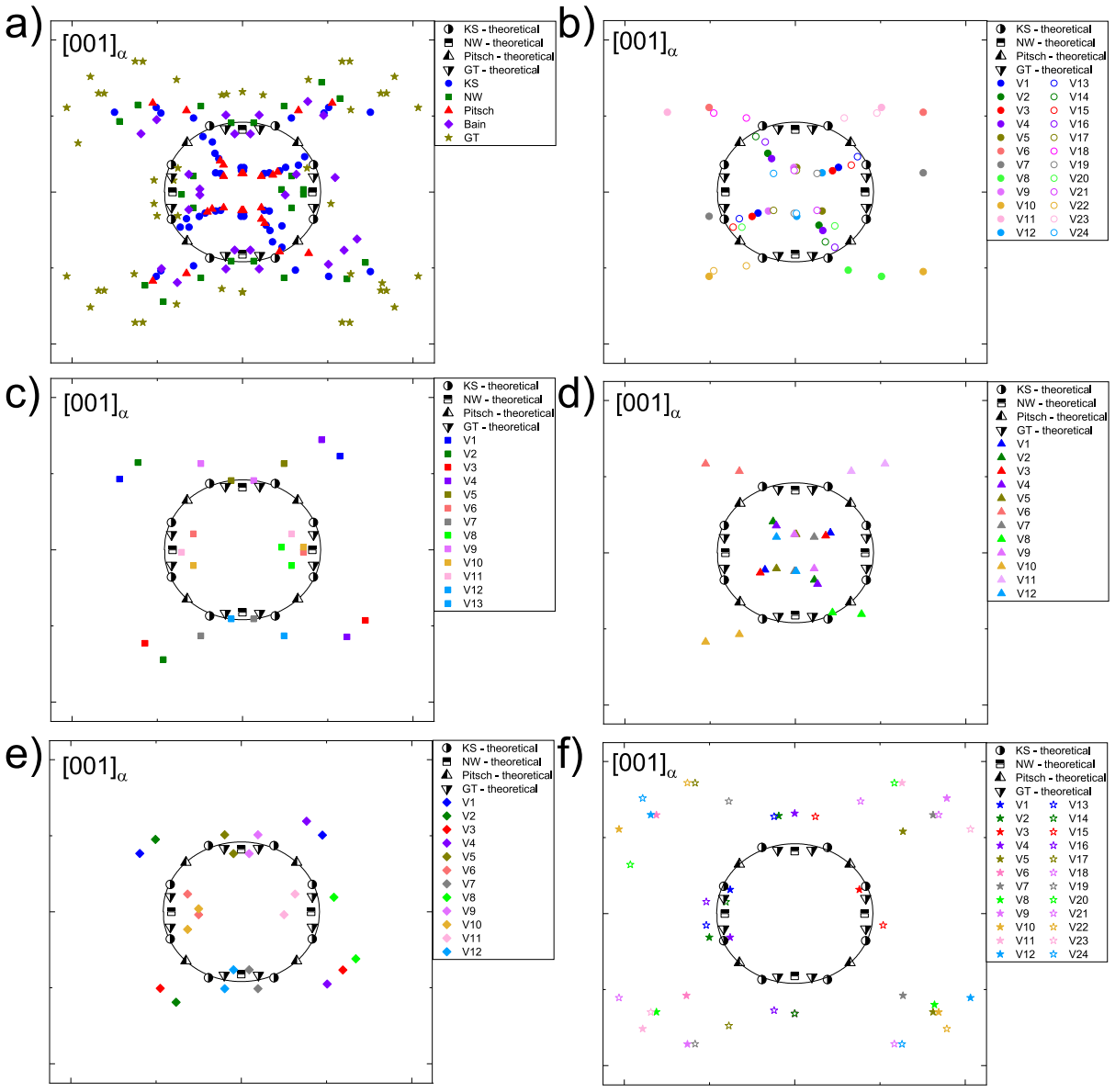

Fig. 8. (a) Pole figure showing ORs as misorientations about $[001]_{BCC}$ for s^{mart}. Variant distribution for (b) KS, (c) NW, (d) Pitsch, (e) Bain-like and (f) GT ORs.

Table 11
Shear displacement and average for s^{bain} and s^{lath}.

OR	s_1^{bain} (nm)	HP_1^{bain} (Cart)	HP_1^{bain} (Miller)	s^{bain} (nm)
KS/P (V1)	[0.08,0.026,−0.063]	(0.45,0.45,0.768)	(3.4 3.4 2)	0.148
KS/P (V13)	[0.02,−0.034,0.023]	(−0.65,−0.65,−0.39)	$(\overline{223.33})$	0.068
NW/B (V1)	[0.026,0.003,−0.04]	(0.63,0.63,0.44)	(2 2 2.86)	0.06
B (V1)	[0.023,0,−0.036]	(0.643,0.643,0.415)	(2 2 3.09)	0.161
B (V13)	[−0.025,−0.048,0.009]	(−0.12,−0.12,−0.98)	$(\bar{1}\ \bar{1}\ \overline{0.12})$	0.188
Average	**[0.025,−0.01,−0.021]**	**(0.64 0.64 0.42)***	**(2 2 3.04)***	**0.125**
OR	s_1^{lath} (nm)	HP_1^{lath} (Cart)	HP_1^{lath} (Miller)	s^{lath} (nm)
KS/P (V1)	[0.10,0.047,−0.179]	(0.61,0.61,0.5)	(5 5 6.1)	0.217
KS/P (V13)	[0.10,0.048,−0.179]	(0.6,0.6,0.51)	(5 5 5.8)	0.326
NW/B (V1)	[0.064,0.041,−0.179]	(0.65,0.65,0.38)	(5 5 8.5)	0.234
B (V1)	[0.065,0.041,−0.179]	(0.65,0.65,0.38)	(5 5 8.5)	0.403
B (V13)	[0.065,0.041,−0.179]	(0.65,0.65,0.38)	(5 5 8.5)	0.414
Average	**[0.079,0.044,−0.0179]**	**(0.635,0.635,0.44)***	**(5 5 7.2)***	**0.318**

computed as:

$$s_j = \sum_{i=0}^{N_B-1} N_{i,j}(a_i + s_i) - a_j,\ j = N_B, \dots, N_A - 1. \quad (16)$$

Only $N_B - 1$ shear vectors s_i are needed and the same solution methods are followed. When comparing Eqs. (4), (15) and (16), we can see that in all cases the number of shear vectors is determined by the dimension of the product phase $\mathcal{B}$.

We apply these results to study shear transformations in FCC→HCP crystals for a targeted number of conditions. For this transition sequence it is widely accepted that stacking $\frac{1}{6}\langle 112\rangle_{FCC}$ Shockley partials on every other FCC plane forms locally an HCP lattice by reversing the stacking sequence. However, an HCP layer may not simply form when a dislocation partial forms in the FCC lattice and an additional driving force is required to promote the phase transformation. So far, no definition of such driving force or its magnitude has been successfully predicted. In addition, other transformation mechanisms have been reported that do not follow the previous dislocation sequence [33]. Such lack of explanation is consistent with previous attempts to predict the crystallography of the transition. Guo et al. [37] studied the crystallography of FCC(γ)→HCP (ϵ) in Fe-Mn-Si alloys. They used Kelly's double-shear version of the PTMC and argued that atomic shuffling on $\{111\}_{FCC}$ planes was necessary for the transformation to happen but did not define the mechanisms for such shuffling. They argued that the introduction of a shuffle parameter is similar to a dilatation parameter but such shuffle effect should be related to the actual driving force for the transformation if there is a dislocation partial already in place [12].

The FCC→HCP transformation in Fe is analysed using the primitive basis for HCP crystals (ϵ) in Table 2 but the primitive basis for V2 in FCC (Table 7) is used for convenience. Substituting vector values in Eq. (15) the following is obtained:

$$\begin{aligned} c_S &= R\left(\frac{a_\gamma}{2}[1,1,0] + \delta^\epsilon \hat{n}_0^\epsilon\right) \\ c_T &= R\left(\frac{a_\gamma}{2}[0,1,1] + s_1^{\epsilon,1}\right) \\ c_U &= R\left(\frac{a_\gamma}{2}[1,0,1] + s_2^{\epsilon,1}\right) \\ c_V &= R\left(\frac{a_\gamma}{2}[2,-1,1] - s_1^{\epsilon,1} + 2s_2^{\epsilon,1} + s_3^{\epsilon,1}\right) \end{aligned} \quad (17)$$

where $\delta^\epsilon = a_\epsilon - \frac{a_\gamma}{\sqrt{2}}$ and $\frac{a_\gamma}{2}[2,-1,1] = -\frac{a_\gamma}{2}[1,1,0]_{FCC} + 2\frac{1}{2}[1,0,1]_{FCC}$, *i.e.* $N_3 = -1$ and $L_3 = 2$, is the non-basis vector for c_V. The last relation corresponds to Eq. (15) where $s_3^{\epsilon,1}$ is the additional shear vector. Fig. 6(b) shows individual shear plots for the results obtained. The curves were calculated fixing $x_1^{\epsilon,1}$ and solving numerically equation (15) in a similar fashion as previous cases; the lattice parameters used for HCP Fe are $a_\epsilon = 0.25$ nm and $\omega = \frac{c_\epsilon}{a_\epsilon} = \sqrt{8/3} \approx 1.633$ [77]. As with the case of FCC→BCC phase transformations, $\boldsymbol{s}_1^{\epsilon,1}$ has only one set of solutions, whereas $\boldsymbol{s}_2^{\epsilon,1}$ and $\boldsymbol{s}_3^{\epsilon,1}$ each have 2 solution sets; $\boldsymbol{s}_1^{\epsilon,1}$ and $\boldsymbol{s}_2^{\epsilon,1}$ are closed curves each having 4 extrema. The curve for $\boldsymbol{s}_1^{\epsilon,1}$ has a minimum (almost equal to zero) at $x_1 \sim 0$ nm; interestingly, the first solution for $\boldsymbol{s}_2^{\epsilon,1}$ (purple dotted line) has virtually identical magnitude as $\boldsymbol{s}_1^{\epsilon,1}$ and the second solution (pink dashed line) is somewhat mirrored about $x_1 \sim 0.10$ nm. $\boldsymbol{s}_3^{\epsilon,1}$ has two constant solutions at ~ 0.149 nm and ~ 0.8 nm. Fig. 6(b) shows the calculations for the total shear considering the 4 possible solutions, 2 for $\boldsymbol{s}_2^{\epsilon,1}$ and 2 for $\boldsymbol{s}_3^{\epsilon,1}$. It is easily seen that the first solution (black line) having $\boldsymbol{s}_2^{\epsilon,1}$ with identical magnitude as $\boldsymbol{s}_1^{\epsilon,1}$ corresponds to the solution with the lowest strain, hence this is considered as the correct solution. We only study the solutions giving the minimum shear for simplicity in the discussions. The predicted shear values for the minimum shear $\boldsymbol{s}^\epsilon$ are $s_1^{\epsilon,1} = [0, -0.0022, -0.0022]$ nm, $s_2^{\epsilon,1} = [-0.0022, 0, -0.0022]$ nm and $s_3^{\epsilon,1} = [-0.11, -0.0589, 0.0589] = \frac{a_\gamma}{6}[\bar{2}\ \bar{1}\ 1] + \tilde{s}_3^{\epsilon,1}$ with $\tilde{s}_3^{\epsilon,1} = [0.0015, 0.007, -0.007]$ nm an excess shear. The model predicts that the transformation occurs via a dislocation partial ($s_3^{\epsilon,1}$) on every other $(1\bar{1}1)_{FCC}$ plane. If $\frac{a_\gamma}{2}[1,1,0]_{FCC}$ and $\frac{a_\gamma}{2}[0,1,1]_{FCC}$ form plane A ($(1\bar{1}1)_{FCC}$), then $s_1^{\epsilon,1}$, $s_2^{\epsilon,1}$ and $s_3^{\epsilon,1}$ respectively lie on planes A ($x - y + z = 0$), B ($x - y + z = a_\gamma$) and C ($x - y + z = 2a_\gamma$). In addition, it predicts that small atomic displacements are necessary for the transition to happen, *i.e.* $s_1^{\epsilon,1}$ and $s_2^{\epsilon,1}$ and the excess strain $\tilde{s}_3^{\epsilon,1}$ correspond to atomic shuffles; although small but these "shuffles" on $(1\bar{1}1)_{FCC}$ and $(\bar{1}11)_{FCC}$ planes are necessary to match the dimensions of the HCP lattice. The total magnitude of the atomic shuffles can be estimated as $\sqrt{(s_1^{\epsilon,1})^2 + (s_2^{\epsilon,1})^2 + (\tilde{s}_3^{\epsilon,1})^2} \approx 0.01$ nm. Therefore, the theory successfully predicts that the classical transformation mechanism of incorporating Shockley partials on every other $\{111\}_{FCC}$ plane plus adding small shuffles on each FCC plane corresponds to the lowest energy configuration for this transition. Lastly, for estimating the OR, the planes for all basis vectors in FCC lie on $(11\bar{1})_{FCC}$ planes, therefore recovering Shoji–Nishiyama's OR (Table 4). The habit planes for $s_1^{\epsilon,1}$, $s_2^{\epsilon,1}$ and $\tilde{s}_3^{\epsilon,1}$ are respectively $(0.57, 0.57, -0.57)_{FCC}$ (or (1 1 $\bar{1}$) in Miller indices), $(0.57, 0.57, -0.57)_{FCC}$ and $(0.075, 0.075, 0.99)_{FCC}$; the predicted values are in agreement with the calculations done by Guo et al. [37].

Interestingly, there is another transformation variant (V2) when considering the following vectors (using a_O, a_P and a_Q as basis vectors):

$$\begin{aligned} c_S &= R\left(\frac{a_\gamma}{2}[1,1,0] + \delta^\epsilon \hat{n}_0^\epsilon\right) \\ c_T &= R\left(\frac{a_\gamma}{2}[0,1,1] + s_1^{\epsilon,2}\right) \\ c_U &= R\left(\frac{a_\gamma}{2}[0,1,-1] + \delta^\epsilon \hat{n}_0^\epsilon - s_2^{\epsilon,2}\right) \\ c_V &= R\left(\frac{a_\gamma}{2}[1,-1,2] - \delta^\epsilon \hat{n}_0^\epsilon + 2s_2^{\epsilon,2} + s_3^{\epsilon,2}\right) \end{aligned} \quad (18)$$

with $s_1^{\epsilon,2} = [-0.036, 0.034, -0.054] = \frac{a_\gamma}{12}[\bar{1}\ 1\ \bar{2}] + [-0.0062, 0.0042, 0.0057] = \frac{a_\gamma}{12}[\bar{1}\ 1\ \bar{2}] + \tilde{s}_1^{\epsilon,2}$, $s_2^{\epsilon,2} = [0.034, -0.036, -0.054] = \frac{a_\gamma}{12}[1\ \bar{1}\ \bar{2}] + [0.0042, -0.0062, 0.0057] = \frac{a_\gamma}{12}[1\ \bar{1}\ \bar{2}] + \tilde{s}_2^{\epsilon,2}$ and $s_3^{\epsilon,2} = [-0.083, 0.0833, 0.0833]$ nm; $s_1^{\epsilon,2}$ and $s_2^{\epsilon,2}$ each represent the sum of $\sim 1/2$ Shockley partial and a small atomic shuffle. $s_1^{\epsilon,2}$ lies on plane A ($x - y + z = 0$), whereas $s_2^{\epsilon,2}$ lies on plane -B ($x - y + z = -a_\gamma$). As for $s_3^{\epsilon,2}$, it lies on plane C ($x - y + z = 2a_\gamma$). This mechanism predicts that the HCP lattice is also reconstructed if 2 half Shockley partials and additional atomic shuffles lie on adjacent $(1\bar{1}1)_{FCC}$ planes, *i.e.* $s_1^{\epsilon,2}$ on A and $s_2^{\epsilon,2}$ on B, with a resulting dilatation also occurring along $[\bar{1}11]_{FCC}$ ($s_3^{\epsilon,2}$). Experimental reports using high-resolution TEM have reported similar mechanisms for the reverse HCP→FCC transformation in cold-rolled Ti [33,80]. It was found that an alternate transformation mechanism consists of coupled glide of two disconnections in adjacent planes with total Burgers vector $\frac{1}{6}\langle 11\bar{2}0\rangle_{HCP}$ along with a shuffle mechanism. For the case of the model, since $s_2^{\epsilon,2}$ lies on -B plane, the Burgers circuit around ABC is calculated as $s_1^{\epsilon,2} - s_2^{\epsilon,2} + s_3^{\epsilon,2} = \frac{a_\gamma}{6}[\bar{2}\ 1\ 1] + [-0.03, 0.09, 0.023] = \frac{a_\gamma}{6}[\bar{2}\ 1\ 1] + \tilde{s}_3^{\epsilon,2}$ nm, *i.e.* 1 Shockley partial and a small atomic shuffle, which is very similar to the reported configuration. We can also estimate the magnitude of the shuffling as $\sqrt{(\tilde{s}_1^{\epsilon,2})^2 + (\tilde{s}_2^{\epsilon,2})^2 + (\tilde{s}_3^{\epsilon,2})^2} \approx 0.14$ nm showing that atomic shuffling is more significant in this configuration; this indicates that the predicted second variant is more difficult to operate due to the higher shear necessary to promote atomic shuffling and can only likely occur under high pressure/mechanical loading conditions; such is consistent with the previous experimental evidence in heavily deformed Ti [80]. This shows that the theory is also able to predict conventional and not conventional transformation mechanisms for FCC→HCP crystals although further work is required to compute all possible atom configurations and crystallographic features of this transition. In addition, the model provides physical and quantitative explanation to the previously ill defined concept of atomic shuffles used in classical theories. Their implications for calculating the driving force are addressed in the following section.

5. Thermodynamic driving force and prediction of transformation start temperatures

The final component of the theory is to link the previous crystallographic results to the Thermodynamics of the various shear transformations. Such will also help in confirming the preliminary conclusions about the various allotropic transformations predicted by the models. A formula for the Thermodynamic driving force in martensite was proposed in previous work [55]. Such equation is based on calculating the elastic strain energy from the transformation at an atomic level using the transformation strain as input parameter: $\Delta G_{strain} = -\frac{(1+\nu)\mu\Delta V}{18(1-\nu)}\bar{\varepsilon}$ with $\bar{\varepsilon} = \left(\frac{\bar{s}}{a}\right)$ the transformation strain, ν Poisson's ratio, μ the shear modulus, a the parent's crystal lattice parameter (a_γ) and ΔV is the volume change induced by the new phase. This equation was derived following Eshelby's model for calculating the elastic energy of a spherical inclusion inserted within a perfect lattice, resulting in additional distortions by the difference in volumes [81]; ΔV was set equal to the molar volume V_m and $\bar{\varepsilon}$ following the work by Cai et al. [82] estimating the strain energy from adding point defects to a perfect lattice, *i.e.* atomic displacements acting as point-like inclusions in a phase transformation. These derivations have been made assuming isotropic distortions from spherical inclusions but distortions are highly anisotropic for the case of shear transformations. Hence, a correction factor α is included in the formula for ΔV: $\Delta V = \alpha V_m \bar{\varepsilon}$. Combining this result with the previous equation, the Thermodynamic driving force is:

$$\Delta G_{strain} = -\frac{\alpha(1+\nu)\mu V_m}{18(1-\nu)}\left(\frac{\bar{s}}{a}\right)^2. \tag{19}$$

$\alpha = 0.02$ was fitted to match the driving force values of different structures and was fixed in all conditions and materials tested. This equation can be used either to compute the local driving force for each transformation variant in a given OR, using the shear values displayed in Tables 7, 8, 10, or to obtain the macroscopic driving force for each transformation. We will focus on the latter since this value can be readily compared against experimental measurements. The start temperatures are calculated by comparing ΔG_{strain} with the Gibbs free energy between the FCC and BCC/HCP phases at different temperatures using the Thermodynamics software Thermocalc and databases TCFe8 and SSOL4; similarly, the parameters used for Eq. (14) are: $\mu = 70$ GPa, $\nu = 0.29$, $V_m = 7.09$ cm^3/mol. Details of the calculations are described in previous work [55]. Table 12 shows prescribed and measured values of ΔG_{strain} in Fe and transformation start temperatures for Widmanstätten ferrite, Bainite, as well as the different martensites. For the case of plate and lenticular martensite, $\bar{s}$ is calculated using the (individual) effective strains $\boldsymbol{s}_i^{k,j}$, which are computed as $(s_i^{k,j})^2 = (\boldsymbol{s}^{twin})^2 - (\tilde{s}_i^{k,j})^2$ with $i = 1,2$, $k = lent, plate$, $j = KS, NW, B$ (as with Table 11), $\boldsymbol{s}^{twin} = \|\frac{a_\gamma}{2}\langle 11\bar{2}\rangle\|$ and $\boldsymbol{s}^{\tilde{k},j} = \sqrt{(\bar{s}_1^{k,j})^2 + (\bar{s}_2^{k,j})^2}$; this is to account only for the net strain necessary following twinning (Eq. (12)). Although no information on the M_s for lenticular martensite was found, experimental reports have shown that lenticular martensite forms in FeNiC ~ 100–150 °C above plate martensite [66,83] and the model successfully lies within this temperature range. More results for HCP→FCC in Fe/Fe10Mn are shown to demonstrate the robustness of the predictions. Two cases are computed one including the total driving force, *i.e.* dislocations+atomic shuffles, and another only considering the atomic shuffles, *i.e.* assuming dislocations form prior to the transformation and only shuffles are required. $\tilde{s}^{\epsilon}$ is calculated by taking the average shear of the 2 variants obtained in Section 4.3; the predicted driving force when only atomic shuffles are considered is lower than the former case indicating that only small lattice distortions are needed to produce the transformation if a dislocation partial is present. The agreement is remarkable in all cases, demonstrating that the present approach is also able to predict and link the transformation strains with the Thermodynamic driving force across material conditions. This also confirms the conclusions about Widmanstätten Ferrite and Bainite.

5.1. Possible links and application of the theory to improve the PTMC

Although several outcomes of this work showed similar predictions to those obtained using the PTMC or similar approaches, making a more direct comparison between methods is difficult. This is because the different assumptions between the two approaches lead to different interpretations of the predictions. Also, we note that different mathematical frameworks can describe the same physical problem, as in the present work and the PTMC, without contradicting themselves. A classical example is Hamiltonian and Lagrangian mechanics, where both theories describe the same physical phenomena but take slightly different approaches (Hamiltonian mechanics uses generalised spatial coordinates, in contrasts to Lagrangian mechanics which uses classical Newtonian descriptions, allowing to describe more complex physical problems using simpler mathematical descriptions). A key assumption in the original PTMC is that two invariant parameters are pre-defined to comply with the OR under consideration, *i.e.* the parallel direction and plane between parent and product phases are established before the transformation sequence starts (Table 1 for FCC→BCC), which only requires solving the transformation matrix for one invariant plane strain (S). In contrast, we only assumed that one variable – the parallel direction – remains invariant in the transformation function T without pre-defining an OR. The invariant planes to define a specific OR were predicted as the planes containing the first and second nearest neighbours to the invariant direction that make the transformation function injective and produce the smallest strain values in T, as indicated in Tables 4–6. This was demonstrated by not only obtaining the expected $\{111\}_{FCC}\|\{110\}_{BCC}$ relationships for the KS and NW ORs but by also predicting (non-closed packed) planes in other ORs, including $\{100\}_{FCC}\|\{111\}_{BCC}$ for Pitsch and $\{100\}_{FCC}\|\{100\}_{BCC}$ for Bain ORs. We therefore have shown that ORs form simultaneously as the transformation takes place – not before – and such relationships are selected to include the directions and planes that minimise the transformation strains.

In addition, by relaxing the assumption of only pre-defining the parallel directions in T, we demonstrated mathematically that two invariant shear displacements are necessary to define the transformation function as injective between FCC→BCC lattices. Such provided a formal justification of why two invariant shear systems are needed in the PTMC to predict main crystallographic features of lath martensite, including the {557} habit plane and $\frac{1}{2}\langle 101\rangle$ interfacial dislocations. We note that although solutions using a single invariant system have been obtained using matrix-based approaches, this does not rule out the possibility of other solutions existing for the same structure. For instance, Baur et al. [19] used a single transformation matrix, *i.e.* considering one invariant shear plane (analogous to P in Eq. (1)), to predict the $\{225\}_{FCC}$ habit plane in plate/lenticular martensite. They demonstrated that the transformation matrix when considering KS OR has 2 habit planes, $\{111\}_{FCC}$ and $\{0.35, 0.35, 0.86\}_{FCC}$; obtaining the $\{111\}_{FCC}$ plane was attributed to the fact that KS OR requires the planes {111} remain invariant, *i.e.* $\{111\}_{FCC}$ are habit planes by definition, but they did not highlight if other solutions exist that also have $\{111\}_{FCC}$ as habit plane. In contrast, the results obtained in this work for lenticular martensite showed (s_i^{lent} in Table 3) that indeed there are 2 habit planes, in cartesian coordinates $(-0.316, -0.316, -0.86)_{FCC}$ and $(-0.596, -0.596, -0.538)_{FCC}$, where the latter is very close to $(111)_{FCC}$; however, these solutions correspond to two compatible twin systems (Eq. (11)). This is interpreted as successfully predicting self-consistent twinning pair-variants using a single transformation function, as experimentally observed but not being fully explained by the PTMC [67]. This example shows how the present approach provides more complete solutions.

The limitations in matrix-based approaches related to the previous assumptions were amplified when studying other crystal lattices with lower symmetries like the HCP lattice. This is because an additional

Table 12
Average shear displacement, Driving Force and Start temperatures in various shear transformations.

Transition	Structure	$\bar{s}$ (nm)	ΔG_{strain} (J/mol) - Mod	ΔG_{strain} (J/mol) - Exp	Start (°C) - Mod	Start (°C) - Exp
FCC→BCC	Widmanstätten F.	0.064	−50	−50 [63]	737	760 [63]
FCC→BCC	Bainite	0.125	−191	−250 [2]	712	690 [84]
FCC→BCC	Lath martensite	0.318	−1,244	−1,000 to −1,250 [55]	545	550 [84]
FCC→BCC	Lent. martensite	0.348	−1,483		510	
FCC→BCC	Plate martensite	0.426	−2,222	−1,800 to −2,100 [85]	407	420 [84]
FCC→HCP (Fe10Mn)	ϵ martensite (disl.+shuffles)	0.157	−301	−270 [86]	118	137 [87]
FCC→HCP	ϵ martensite (shuffles)	0.077	−72	−68 to −90 [87,88]		

concept of atomic shuffle is required to make Eq. (1) injective, in addition to considering 2 shear invariant systems. Although a physical interpretation has been given to this concept, it lacks a self-contained mathematical formalism. In contrast, our mathematical formalism was able to justify the need of adding another shear component to make T injective in FCC→HCP (Eq. (17)). Similar to the FCC→BCC lattice transformation case, the theory not only predicted that the transformation happens by forming dislocation partials on every other $\{111\}_{FCC}$ plane – without pre-defining their existence – but it was shown that other mechanisms reported in the literature can happen. Although T in Eq. (3) could be represented in matrix form to establish more analogies to P in Eq. (1), such conversion may not provide more insights than its vector form. This is because purely crystallographic criteria are adopted to compute P and there is no way to verify whether the solutions to this problem are energetically favourable. Considering the extremum principle allowed us to link the crystallography of relevant transformation processes in Fe with the associated Thermodynamic driving force and crystal defects.

The main aim of this work was to introduce an alternative theory and apply in pure allotropic materials like Fe. Alloying additions not only modify the lattice parameter but can promote additional lattice distortions, *e.g.* C in Fe or Al in Ti, which can change the crystallography and associated crystal defects of shear transformations, *e.g.* C changes the frequency of variant pairing in lath martensite [89]. Similarly, the Thermodynamics of the transformation will change as the local strain values increase with alloying [55]. These features would need to be incorporated the model but such lies beyond the scope of the work. Nonetheless, this will be addressed in future publications.

In summary, following relevant modifications in the basic assumptions of matrix-based theories, it may be possible to improve the existing results from the PTMC by means of linking crystallography with Thermodynamics and connecting results of the various shear transformations in Fe that, until now, remained disconnected. Modifications include using a relaxed assumption of only defining one invariant direction and not invariant planes and include an energy-based criterion – like the extremum principle – to compensate for a missing variable when computing P. In addition, should be acknowledged that the number of invariant shear systems to define the transformation matrix as injective is correlated to the dimension – or number of lattice points required to generate the motif – of the parent and product lattices.

6. Summary and concluding remarks

A new theory for predicting shear transformations in crystalline materials has been introduced. It is presented as an alternative approach to classical theories to explain and unify results in several transformations using the same formalism. The crystal lattice and shear transformations were treated as vector space and vector functions respectively to overcome longstanding challenges of previous theories for the crystallography of shear transformations. A shear transformation function T was defined as a linear function containing 1 invariant direction (dilatation) and the remaining vectors were atom (shear) displacement functions matching the dimensions of the number of vectors forming the motif, 3 for FCC and BCC crystals and 4 for HCP crystals. The extremum principle was used to obtain the atomic displacement paths minimising and maximising the strain energy from all possible vector solutions. A main reason why atomic (shear) displacements were considered instead of unitless strain values is because the choice of the reference length to compute the strain, *e.g.* dividing by the interplanar distances, can be arbitrary and not provide more insights of specific atomic trajectories during the transformation, as atomic displacements are not necessarily parallel to the reference distance. An example is when computing the crystal defects forming during the transformation, e.g. twinning in Eq. (12); it was possible to split the total displacements into a $\frac{a_\gamma}{2}\langle 112\rangle$ deformation twin and additional atomic displacements required to fully transform into martensite, *i.e.* local driving force; such would not have been possible to elucidate out if we had considered unitless strains in the analysis. The theory predicts that commonly observed defects, including dislocations and twins, simultaneously form as the new phase emerges, which enable efficient strain accommodation processes. Orientation relationships were obtained by finding suitable vector combinations producing the lowest distortions between invariant directions in the parent and product phases; the model not only was successful in predicting common ORs between FCC→BCC, BCC→HCP and FCC→HCP crystals but it also allowed connecting such crystallographic features with different atomic paths involved in the transformations and their associated energetics. Transformations taking place in the FCC→BCC crystal system in Fe were used as case study to highlight the main features of the theory as well as to demonstrate its novelty. Different vector combinations representing basis vectors for the transformation function were explored demonstrating that those with lowest dilatation and shear energy correspond to the transformation variants for a given OR. Lastly, the results were linked to a Thermodynamic model to predict the local or macroscopic driving force, where the latter was computed using the average shear strains of the predicted extrema.

The theory was later extended to cover transformations between crystal lattices of different dimensions. Targeted validation of the FCC→HCP crystal transformation was addressed. Similar analysis can be done for the remaining transformations in FCC↔BCC↔HCP crystals not only in Fe but also other relevant materials such as Ti and Zr. The theory is also readily available to study other transformations like twinning by assigning as parent phase a “twinned” mirrored structure. In addition, the theory can describe transformations in ordered systems such as NiTi. Although the theory was validated in pure Fe, it can easily account for elemental effects, as it is well known that chemical composition affects the crystallography and microstructure of shear transformations, *e.g.* C in Fe and also for complex materials undergoing various transformations like high-entropy alloys [90]. This could be addressed by including additional vector functions in the transformation function representing different atomic species as well as extending the hard-sphere dilatation criterion to account for additional solute distortions/obstruction affecting specific invariant directions; the latter could alter the occurrence of some ORs or even predict new ones. This could be done and expanded in future work. In addition, the theory can be very useful to help improving existing interatomic potentials by

providing new information about possible atomic paths for different ORs and transformation structures [28,91,92]. Finally, although the predicted transformation start temperatures have been obtained considering the extrema values in the shear transformation function, it is well known that structures like Bainite can form isothermally between B_s and M_s, also leading to different crystallography and transformation kinetics; this means that the shear processes involved and associated driving force should lie between $\boldsymbol{s}^{bain,j}$ and $\boldsymbol{s}^{mart,j}$ in the curves computed for each OR case, *e.g.* Fig. 2, but additional considerations on the transformation kinetics are needed to predict the times required for the start of the transformation. Such can be done by combining the results of the present theory with coarse graining atomistic methods, such as kinetic Monte Carlo, allowing the prescription of kinetic processes taking place after long times (>ms).

In summary, the following conclusions can be drawn from this work:

- We have developed an integrated approach that answered holistically several questions that were not possible to address before using classical phenomenological and matrix-based approaches: By using a vector formalism for the crystal lattice, we can explain the atomic trajectories of well-known transformations in Fe and their associated crystal defects. Previous matrix-based theories had to assume specific crystal defects to reproduce experimental results, therefore limiting their predictability. The Extremum principle provided an energy-based framework to explain why multiple shear transformations happen in Fe based on the strain energy from atomic displacements, with direct connection to their atomic trajectories and Thermodynamics. The combination of these methods provided a mathematical formalism to predict and explain why several Orientation Relationships (ORs) have been observed experimentally. Our previously developed thermodynamic model linked the predicted crystallographic features with the driving force of the transformation, hence predicting the start temperature of several shear transformations, *i.e.* Bainite, Widmanstäten ferrite, lath martensite, plate martensite, and lenticular martensite; before this work, where there was no physics-based model that could unify their mechanisms and predicted Thermodynamic properties. The new theory is able to link the local and macroscopic crystallographic features of shear transformations in crystalline materials with the atomic-scale mechanisms and Thermodynamics. The combination of these features enabled the simultaneous prediction of the most relevant transformations in Fe, namely Widmansttätten Ferrite, Bainite, lath martensite, plate martensite as well as lenticular martensite. To the authors' knowledge, this is the first theory able to unify our understanding about such transitions, addressing unanswered – or partially answered – questions about shear transformations in Fe.
- It is predicted that Widmanstäten Ferrite corresponds to the local minimum energy configuration for either KS and NW ORs with total atomic shear displacement as slow as ~ 0.06 nm – or a strain of 0.178 – involved in the transformation process.
- The theory indicates that Bainite corresponds to the macroscopic minimum energy configuration also forming as a bulk phase with average shear displacements of ~ 0.125 nm – or strain of 0.35 – and mean habit plane $\{223\}_{FCC}$. $\langle 10\bar{1}\rangle_{FCC}$ defects are predicted to form simultaneously as the new phase emerges as resulting structure. In addition, the driving force successfully predicted the Bainite start temperature and the theory in principle can also be used to compute the driving force under isothermal conditions between B_s and M_s; such can be done by calculating the average strains along the shear curves between the extrema for Bainite and Martensite (*e.g.* Fig. 2(d) or Fig. 6(a)). However, modelling of phase kinetics is also required to determine the critical time for the transformation.
- The theory predicts that lath martensite corresponds to shear configurations minimising atomic displacements when there is no other driving force, such as diffusion, with average shear displacements of ~ 0.318 nm- or 0.88 strain. It was also demonstrated that $\frac{1}{2}\langle 10\bar{1}\rangle$ dislocations form simultaneously as the phase transformation takes place. In addition, all local habit planes reported for lath martensite were successfully predicted and the macroscopic habit plane corresponds to $\{557\}_{FCC}$.
- The maximum shear energy configurations correspond to lenticular and plate martensite both forming twins to accommodate the transformation strains but also including excess strains; the average shear displacements were 0.348 nm – or 0.97 strain – and 0.426 nm – or 1.19 strain – for lenticular and plate martensite, respectively. It was shown that plate martensite contains mostly twins as this structure accommodates more effectively the strains from the transformation, whereas lenticular martensite can also form tangled dislocations to compensate for the excess strain from twinning. The excess shear corresponded to the effective shear strain to calculate the driving force. As with lath martensite, the theory predicted that in twinning, additional atomic shear displacements and the phase transition occur simultaneously.
- Commonly reported ORs in Fe were predicted, *i.e.* Kurdjumov–Sachs, Nishiyama–Wasserman, Pitsch and Greninger–Troiano. In addition, a Bain-like orientation relationship was also predicted rectifying Bain's OR requirements and as it only involves fixing 1 invariant direction. By solving the transformation function for all possible atom direction combinations, the theory confirmed the empirical argument that several ORs form within a single variant during the transformation and that there is no preference for one or more ORs to form, as the shear strains are similar in most cases. In addition, by plotting the transformation paths as misorientations between orientations of the parent and product phases, it was shown that there are direct paths connecting variants in all ORs.
- Targeted results for FCC→HCP in Fe demonstrated that the theory is applicable to other shear transformations. The theory not only successfully predicted that the classical mechanism of incorporating 1 Shockley partial on every other $\{111\}_{FCC}$ plane corresponds to the lowest energy configuration for this transition but it was able to predict unconventional transformation mechanisms reported experimentally. In addition, the theory provides physical and quantitative explanation to the previously ill-defined concept of "atomic shuffles" used in classical theories, as well as their implications for calculating the driving force. Specifically, the shear magnitude of the shuffles corresponds to the Thermodynamic driving force when dislocation partials are already present.

CRediT authorship contribution statement

Enrique Galindo-Nava: Conceptualization, Data curation, Formal analysis, Funding acquisition, Investigation, Methodology, Project administration, Resources, Software, Validation, Visualization, Writing.

Declaration of competing interest

The authors declare that they have no known competing financial interests or personal relationships that could have appeared to influence the work reported in this paper.

Acknowledgements

The author would like to acknowledge the Royal Academy of Engineering for his Research Fellowship funding.

Appendix

Table 13 shows values predicted for first and second nearest neighbours of representative directions in FCC, BCC and HCP lattices and

Table 13
First and second nearest neighbours along special directions in the FCC, BCC and HCP lattices.

Structure	Dir.	1NN	Plane	2NN	Plane
FCC	$\frac{1}{2}[110]$	$\frac{1}{2}[011]$, $\frac{1}{2}[10\bar{1}]$, $\frac{1}{2}[21\bar{1}]$, $\frac{1}{2}[121]$ $\frac{1}{2}[01\bar{1}]$, $\frac{1}{2}[101]$, $\frac{1}{2}[211]$, $\frac{1}{2}[12\bar{1}]$	$(1\bar{1}1)$ $(\bar{1}11)$	[100] [010]	(001)
	$\frac{1}{2}[211]$	$\frac{1}{2}[101]$, $\frac{1}{2}[110]$, $\frac{1}{2}[312]$, $\frac{1}{2}[321]$	$(\bar{1}11)$	[100], [111]	$(0\bar{1}1)$
	[100]	$\frac{1}{2}[110]$, $\frac{1}{2}[1\bar{1}0]$, $\frac{1}{2}[310]$, $\frac{1}{2}[3\bar{1}0]$	(001)	$\frac{1}{2}[211]$, $\frac{1}{2}[2\bar{1}1]$	$(0\bar{1}1)$
		$\frac{1}{2}[101]$, $\frac{1}{2}[10\bar{1}]$, $\frac{1}{2}[301]$, $\frac{1}{2}[30\bar{1}]$	(010)	$\frac{1}{2}[2\bar{1}1]$, $\frac{1}{2}[21\bar{1}]$	(011)
BCC	$\frac{1}{2}[111]$	[100], [010], [011], [101]	(110)	$\frac{1}{2}[3\bar{1}1]$, $\frac{1}{2}[\bar{1}31]$	(110)
		[001], [110]	$(1\bar{1}0)$	$\frac{1}{2}[1\bar{1}3]$, $\frac{1}{2}[13\bar{1}]$	(200)
				$\frac{1}{2}[31\bar{1}]$, $\frac{1}{2}[\bar{1}13]$	(020)
	[100]	$\frac{1}{2}[111]$, $\frac{1}{2}[11\bar{1}]$, $\frac{1}{2}[3\bar{1}1]$, $\frac{1}{2}[3\bar{1}\bar{1}]$ $\frac{1}{2}[1\bar{1}1]$, $\frac{1}{2}[1\bar{1}\bar{1}]$, $\frac{1}{2}[31\bar{1}]$, $\frac{1}{2}[311]$	(110) $(1\bar{1}0)$	[110], [101], [10$\bar{1}$], [1$\bar{1}$0]	(100)
	[110]	$\frac{1}{2}[111]$, $\frac{1}{2}[11\bar{1}]$, $\frac{1}{2}[33\bar{1}]$, $\frac{1}{2}[331]$	$(1\bar{1}0)$	[100], [120]	(100)
				[010], [210]	(010)
HCP	$[10\bar{1}0]$	$[1\bar{1}00]$, $[0\bar{1}10]$, $[11\bar{2}0]$, $[21\bar{1}0]$	(0001)	$\frac{1}{6}[44\bar{6}3]$	$(\bar{2}\bar{2}32)$
		$\frac{1}{6}[42\bar{6}3]$, $\frac{1}{6}[10\ 2\ \bar{12}\ 3]$	$(12\bar{3}1)$	$\frac{1}{6}[44\bar{6}\bar{3}]$	$(12\bar{3}2)$
		$\frac{1}{6}[42\bar{6}\bar{3}]$, $\frac{1}{6}[10\ 2\ \bar{12}\ \bar{3}]$	$(\bar{1}231)$		

their respective planes. Calculations for HCP crystals have been conducted assuming ideal $\omega = \frac{c_\epsilon}{a_\epsilon} = \sqrt{\frac{8}{3}}$.

References

[1] H. Bhadeshia, R. Honeycombe, Steels: Microstructure and Properties, Butterworth-Heinemann, 2006.
[2] H. Bhadeshia, Bainite in Steels: Theory and Practice, CRC Press, 2015.
[3] G. Olson, Genomic materials design: The ferrous frontier, Acta Mater. 61 (2013) 771–781.
[4] Z. Li, C. Tasan, K. Gokuldoss Pradeep, D. Raabe, A TRIP-assisted dual-phase high-entropy alloy: Grain size and phase fraction effects on deformation behaviourl, Acta Mater. 131 (2017) 323–335.
[5] L. Fielding, The bainite controversy, Mater. Sci. Tech. 29 (2013) 383–399.
[6] V. Tong, S. Joseph, A. Ackerman, D. Dye, T. Britton, Using transmission Kikuchi diffraction to characterised α variants in an $\alpha+\beta$ titanium alloy, J. Micros. 267 (2017) 318–329.
[7] C. Cayron, What EBSD and TKD Tell Us about the Crystallography of the Martensitic B2-B19' Transformation in NiTi Shape Memory Alloys, Crystals 10 (2020) 562.
[8] J. Chevalier, L. Gremillard, The tetragonal-monoclinic transformation in Zirconia: Lessons learned and future trends, J. Am. Ceram. Soc. 92 (2009) 1901–1920.
[9] N. Navruz, Crystallography of the tetragonal-to-monoclinic phase transformation in ceria-zirconia, Phase Trans. 78 (2005) 539–545.
[10] K. Verbeken, L. Barbé, D. Raabe, Evaluation of the crystallographic orientation relationships between FCC and BCC phases in TRIP steels, ISIJ Int. 49 (2009) 1601–1609.
[11] P. Thome, M. Schneider, V. Yardley, E. Payton, G. Eggeler, Crystallographic analysis of plate and lath martensite in Fe-Ni alloys, Crystals 12 (2022) 156.
[12] J. Bowles, J. Mackenzie, The crystallography of martensite transformations I, Acta Metall. 2 (1954) 129–137.
[13] T. Tadaki, Phenomenological consideration on the change from the non-thermoelastic to the thermoelastic type of martensitic transformations in Fe_3Pt alloy, Trans. JIM 18 (1977) 864–870.
[14] A. Acton, M. Bevis, A generalised martensite crystallography theory, Mater. Sci. Eng. 5 (1969) 19–29.
[15] N. Ross, A. Crocker, A generalized theory of martensite crystallography and its application to transformations in steels, Acta Metall. 18 (1970) 405–418.
[16] N. Zolotorevsky, A. Zisman, Crystallography of martensitic transformation in steels: Advances in experimental and theoretical research, Rev. Adv. Mater. Tech. 2 (2020) 39–50.
[17] C. Cayron, One-step model of the face-centred-cubic to body-centred-cubic martensitic transformation, Acta Cryst. 69 (2013) 498–509.
[18] C. Cayron, Continuous atomic displacements and lattice distortion during fcc-bcc martensitic transformation, Acta Mater. 96 (2015) 189–202.
[19] A. Baur, C. Cayron, R. Logé, $\{225\}_\gamma$ habit planes in martensitic steels: From the PTMC to a continuous model, Sci. Rep. 7 (2017) 40938.
[20] C. Cayron, Shifting the shear paradigm in the crystallographic models of displacive transformations in metals and alloys, Crystals 8 (2018) 181.
[21] J. Hirth, R. Pond, Compatibility and accomomdation in displacive phase transformations, Prog. Mater. Sci. 56 (2011) 586–636.
[22] M. Zhang, P. Kelly, Edge-to-edge matching and its applications Part I. application to the simple HCP/BCC system, Acta Mater. 53 (2005) 1073–1084.
[23] M. Zhang, P. Kelly, Edge-to-edge matching and its applications Part I. application to Mg-Al, Mg-Y and Mg-Mn alloys, Acta Mater. 53 (2005) 1085–1096.
[24] A. Gautam, J. Howe, A method to predict the orientation relationship, interface planes and morphology between a crystalline precipitate and matrix. Part I. Approach, Phil. Mag. 91 (2011) 3203–3227.
[25] A. Gautam, J. Howe, A method to predict the orientation relationship, interface planes and morphology between a crystalline precipitate and matrix. Part I. application, Phil. Mag. 93 (2013) 3472–3490.
[26] F. Maresca, W. Curtin, The Austenite/lath martensite interface in steels: Structure, athermal motion, and in-situ transformation strain revealed by simulation and theory, Acta Mater. 134 (2017) 302–323.
[27] M. Müller, P. Erhart, K. Albe, Analytic bond-order potential for bcc and fcc iron-comparison with established embedded-atom method potentials, J. Phys.: Condens. Matter 19 (2007) 326220.
[28] X. Ou, Molecular dynamics simulations of fcc-to-bcc transformation in pure iron: A review, Mater. Sci. Tech. 33 (2017) 822–835.
[29] P. Kelly, Crystallography of lath martensite in steels, Mater. Trans. 33 (1992) 235–242.
[30] C. Wayman, The phenomenological theory of martensite crystallography: Interrelationships, Metall. Mater. Trans. A 25 (1994) 1787–1795.
[31] K. Staudhammer, L. Murr, S. Hecker, Martensitic (b.c.c.) embryos and substructure in stainless steel: A transmission electron microscope study, Acta Metall. 31 (1983) 267–274.
[32] T. Song, B. De Cooman, Martensite nucleation at grain boundaries containing intrinsic grain boundary dislocations, ISIJ Int. 54 (2014) 2394–2403.
[33] X. Yang, S. Sun, H. Ruan, S. Shi, T. Zhang, Shear and shuffling accomplishing polymorphic fcc $\gamma \rightarrow$ hcp $\epsilon \rightarrow$ bct α martensitic phase transformation, Acta Mater. 136 (2017) 347–354.
[34] J. Liu, D. Kaoumi, Use of in-situ TEM to characterize the deformation-induced martensitic transformation in 304 stainless steel at cryogenic temperature, Mater. Charac. 136 (2018) 331–336.
[35] K. Koumatos, A. Muehlemann, A theoretical investigation of orientation relationships and transformation strains in steels, Acta Cryst. 73 (2017) 115–123.
[36] H. Liu, X. Cheng, N. Valanoor, Universal approach for predicting crystallography of heterogeneous epitaxial nanocrystals with multiple orientation relationships, Appl. Mater. Interfaces 8 (2016) 34844–34853.
[37] Z. Guo, Y. Rong, S. Chen, T. Hsu, Crystallography of FCC(γ) $\rightarrow$HCP(ϵ) martensitic transformation in Fe-Mn-Si based alloys, Scr. Mater. 41 (1999) 153–158.
[38] J. Christian, Analyses of lattice and shape deformations and of atomic shuffles in martensitic transformation, Mater. Sci. Eng. A 127 (1990) 215–227.
[39] H. Burzlaff, H. Grimmer, B. Bruber, P. de Wolff, H. Zimmermann, Crystal lattices, in: International Tables for Crystallography A, Chapter 3.1, 2016, pp. 698–719.
[40] E. Bain, N. Dunkirk, The nature of martensite, Trans. AIME 70 (1924) 25.
[41] U. Dahmen, Orientation relationships in precipitation systems, Acta Metall. 30 (1982) 63–73.
[42] C. Luo, G. Weatherly, The invariant line and precipitation in a Ni-45 wt% Cr alloy, Acta Metall. 8 (1987) 1963–1972.
[43] X. Chen, Y. song, N. Tamura, R. James, Determination of the stretch tensor for structural transformations, J. Mech. Phys. Solids 93 (2016) 34–43.
[44] K. Koumatos, A. Muehlemann, Optimality of general lattice transformations with applications to the bain strain in steel, Proc. R. Soc. Lond. Ser. A Math. Phys. Eng. Sci. 472 (2016) 20150865.
[45] K. Koumatos, A. Muehlemann, A parameter free double shear theory for lath martensite, Acta Cryst. 75A (2019) 866–875.
[46] J. Ball, Mathematical models of martensitic microstructure, Mater. Sci. Eng. A 378 (2004) 61–69.
[47] K. Bhattacharya, Microstructure of Martensite: Why It Forms and how It Gives Rise to the Shape-Memory Effect, Oxford series on materials modelling, 2003.
[48] J. Basdevant, Variational Principles in Physics, Springer, 2006.

[49] F. Fischer, J. Svoboda, H. Petryk, Thermodynamic extremal principles for irreversible processes in materials science, Acta Mater. 67 (2014) 1–20.
[50] J. Svoboda, Y. Shan, E. Kozeschnik, F. Fischer, A thermokinetic model for Mg-Si couple formation in Al-Mg-Si alloys, Modelling Simul. Mater. Sci. Eng. 24 (2016) 035021.
[51] M. Bonvalet-Rolland, T. Philippe, J. Agren, Kinetic theory of nucleation in multicomponent systems: An application of the thermodynamic extremum principle, Acta Mater. 171 (2019) 1–7.
[52] F. De Angelis, Multifield pootentials and derivation of extremum principles, Mater. Sci. Forum 539–543 (2007) 2625–2630.
[53] D. Djukić, T. Atanacković, An always extremum variational principle for classical mechanics via a canonical transformation, Int. J. Non-Linear Mech. 25 (1990) 583–595.
[54] J. Taylor, A global extremum principle for the analysis of solids composed of softening material, Int. J. Solids Struct. 30 (1993) 2057–2069.
[55] E. Galindo-Nava, On the prediction of martensite formation in metals, Scr. Mater. 138 (2017) 6–11.
[56] J. Watson, P. McDougall, The crystallography of Widmanstätten ferrite, Acta Metall. 21 (1973) 961–973.
[57] B. Sandvik, C. Wayman, Characteristics of lath martensite: Part III. Some theoretical considerations, Metall. Trans A 14 (1982) 836–844.
[58] S. Morito, Y. Adachi, T. Ohba, Morphology and crystallography of sub-blocks in ultra-low carbon lath martensite steel, Mater. Trans. 50 (2009) 1919–1923.
[59] J. Rigsbee, H. Aaronson, The interfacial structure of the broad faces of ferrite, Acta Metall. 27 (1979) 365–376.
[60] D. Phelan, R. Dippenaar, Widmanstätten ferrite plate formation in low-carbon steels, Metall. Mater. Trans. A 35 (2004) 3701–3706.
[61] L. Cheng, X. Wan, K. Wu, Three-dimensional morphology of grain boundary Widmanstätten ferrite in a low carbon low alloy steel, Mater. Charact 61 (2010) 192–197.
[62] Y. He, S. Godet, J. Jonas, Observations of the Gibeon meteorite and the inverste Greninger-Troiano orientation relationship, J. App. Crys. 72 (2006) 72–81.
[63] A. Ali, H. Bhadeshia, Nucleation of Widmanstätten ferrite, Mater. Sci. Tech. 6 (1990) 781–784.
[64] A. Zisman, Unique properties of habit plane {557} in origination of lath martensite, Mater. Lett. 275 (2020) 128140.
[65] H. Sato, S. Zaefferer, A study on the formation mechanisms of butterfly-type martensite in Fe-30% Ni alloy using EBSD-based orientation microscopy, Acta Mater. 57 (2009) 1931–1937.
[66] M. Umemoto, E. Yoshitake, I. Tamura, The morphology of martensite in Fe-C, Fe-Ni-C and Fe-Cr-C alloys, J. Mater. Sci. 18 (1983) 2893–2904.
[67] Y. Shinohara, S. Akabane, T. Inamura, Analysis of variant-pairing tendencies in lenticular martensite microstructures based on rank-1 connection, Sci. Rep. 11 (2021) 14957.
[68] A. Shibata, T. Murakami, S. Morito, T. Furuhara, T. Maki, The origin of midrib in lenticular martensite, Mater. Trans. 49 (2008) 1242–1248.
[69] W. Song, D. Carsten, E. Galindo-Nava, Carbon redistribution in martensite in high-C steel: Atomic-scale characterization and modelling, Metals 8 (2018) 577.
[70] K. Ogawa, S. Kajiwara, High-resolution electron microscopy study of ledge structures and transition lattices at the austenite-martensite interface in Fe-based alloys, Phil. Mag. 84 (2004) 2919–2947.
[71] T. Chiba, G. Miyamoto, T. Furuhara, Comparison of variant selection between lenticular and lath martensite transformed from deformed austenite, ISIJ Int. 53 (2013) 915–919.
[72] A. Bogers, W. Burgers, Partial dislocations on the {110} planes in the B.C.C. lattice and the transition of the F.C.C. into the B.C.C. lattice, Acta Metall. 12 (1964) 255–261.
[73] G. Olson, M. Cohen, A mechanism for the strain-induced nucleation of martensitic transformations, J. Less Comm. Metals 28 (1972) 107–118.
[74] M. Visotin, I. Tarasov, A. Fedorov, S. Varnakov, S. Ovchinnikov, Prediction of orientation relationship and interface structure between α-, β- and γ–$FeSi_2$ and Si phases, Acta Crystallogr. Sect. B 76 (2020) 469–482.
[75] P. Kelly, M. Zhang, Edge-to-edge matching- the fundamentals, Metall. Mater. Trans. A 37 (2006) 833–839.
[76] Y. Matsukawa, I. Okuma, H. Muta, Y. Shinohara, R. Suzue, H. Yang, T. Maruyama, T. Toyama, J. Shen, Y. Li, Y. Satoh, S. Yamanaka, H. Abe, Crystallographic analysis on atomic-plane parallelisms between bcc precipitates and hcp matrix in recrystallized Zr-2.5Nb alloys, Acta Mater. 126 (2017) 86–101.
[77] S. Merkel, A. Lincot, S. Petitgirard, Microstructural effects and mechanism of bcc-hcp-bcc transformations in polycrystalline iron, Phys. Rev. 102 (2020) 104103.
[78] P. Xie, S. Shen, C. Wu, J. Chen, Abnormal orientation relation between fcc and hcp structures revealed in a deformed high manganese steel, J. Mater. Sci. Tech. 60 (2021) 156–161.
[79] C. Cayron, EBSD imaging of orientation relationships and variant groupings in different martensitic alloys and Widmanstätten iron meteorites, Mater. Charac. 94 (2014) 93–110.
[80] H. Wu, A. Kumar, J. Wang, X. Bi, C. Tomé, Z. Zhang, S. Mao, Rolling-induced face centered cubic titanium in hexagonal close packed titanium at room temperature, Sci. Rep. 6 (2016) 24370.
[81] J. Eshelby, Distortion of a crystal by point imperfections, J. Appl. Phys. 25 (1954) 255.
[82] W. Cai, R. Sills, D. Barnett, W. Nix, Modeling a distribution of point defects as misfitting inclusions in stressed solids, J. Mech. Phys. Sol. 66 (2014) 154–171.
[83] C. Magee, R. Davies, The structure, deformation and strength of ferrous martensites, Acta Metall. 19 (1971) 345–354.
[84] E. Wilson, $\gamma \rightarrow \alpha$ transformation in Fe, Fe-Ni, and Fe-Cr alloys, Metal Sci. 18 (1984) 471–484.
[85] A. Borgenstam, M. Hillert, Driving force for fcc.→b.c.c. martensites in Fe-X alloys, Acta Mater. 5 (1997) 2079–2091.
[86] K. Ishida, Effect of alloying elements on the critical driving force of martensitic transformation in iron alloys, Scripta Metall. 11 (1977) 237–242.
[87] Y. Lee, C. Choi, Driving force for $\gamma \rightarrow \epsilon$ martensitic transformatoin and stacking fault energy of γ in Fe-Mn binary system, Metall. Mater. Trans. A 31 (2000) 355–360.
[88] S. Cotes, A. Fernández Guillermet, M. Sade, Phase stability and fcc/hcp martensitic transformation in Fe-Mn-Si alloys: Part II. Thermodynamic modelling of the driving forced and the M_s and A_s temperatures, J. Alloy Comp. 280 (1998) 168–177.
[89] A. Stormvinter, A. Borgenstam, J. Agren, Thermodynamically based prediction of the martensite start temperature for commercial steels, Metall. Mater. Trans A 43 (2012) 3870–3879.
[90] L. de Jeer, V. Ocelík, J. De Hosson, Orientation relationships in $Al_0.7CoCrFeNi$ High-Entropy Alloy, Microsc. Microanal. 23 (2017) 905–915.
[91] S. Tateyama, Y. Shibuta, T. Suzuki, A molecular dynamics study of the fcc-bcc phase transformation kinetics of iron, Acta Mater. 59 (2008) 971–974.
[92] L. Sandoval, H. Urbassek, P. Entel, The bain versus Nishiyama-Wassermann path in the martensitic transformation of Fe, New J. Phys. 11 (2009) 103027.